NTNU – Trondheim
Norwegian University of
Science and Technology

Micro-photoluminescence spectroscopy of self-catalyzed zincblende GaAs nanowires grown by molecular beam epitaxy

Terje Sund Mjåland

Master of Science in Electronics
Submission date: June 2012
Supervisor: Helge Weman, IET

Norwegian University of Science and Technology
Department of Electronics and Telecommunications

μ-Photoluminescence spectroscopy of self-catalyzed zincblende GaAs nanowires grown by molecular beam epitaxy

Terje Mjåland
NTNU - Norwegian University of Science and Technology
Department of Electronics and Telecommunications

June 25, 2012

Abstract

In this thesis, single zincblende GaAs nanowires grown by molecular beam epitaxy using the self-catalyzed approach were studied with μ-photoluminescence spectroscopy in order to assess the optical quality of self-catalyzed GaAs nanowires grown for the first time at NTNU and to compare the optical properties of self-catalyzed GaAs nanowires with Au-assisted GaAs nanowires and bulk GaAs references. The low temperature and temperature dependence measurements revealed type II recombinations between zincblende and wurtzite segments occurring at the nanowire tips, however it was established that radiative recombination does not take place in the zincblende GaAs nanowire core. As the thesis progressed, valuable feedback was given to the growers in order to optimize nanowire growth conditions. The thesis builds upon data from earlier work within this project and provides a foundation for future work on self-catalyzed GaAs nanowire devices at NTNU.

Acknowledgements

This thesis is submitted in partial fulfilment on the requirements for the Master of Science degree in nanoelectronics and photonics at the Norwegian University of Technology and Science (NTNU) during spring 2012. The experiments have been performed in the nanophotonics lab with Ph.D student Lyubomir Ahtapodov as supervisor at the Department of Electronics and Telecommunication.

First of all I would like to thank Prof. Helge Weman for including me in the group and giving me the opportunity to do research on the exciting new field which is nanowires.

I would like to thank Lyubomir Ahtapodov for his patience teaching me in the field of nanowires and helping me performing the experiments. Further, I am grateful to Abdul Mazid Munshi and Dheeraj Dasa for their help on my theory section about molecular beam epitaxy and nanowire synthesizing.

Finally, I want to thank my family for supporting my education by showing interest and encouragement.

Terje Sund Mjåland
Trondheim, Norway
June 2012

Nomenclature

AlGaAs	Aluminium Gallium Arsenide
BEC	Bound Exciton Complex
CCD	Charge Coupled Device
EHP	Electron Hole Plasma
FWHM	Full Width at Half-Maximum
GaAs	Gallium Arsenide
IQE	Internal Quantum Efficiency
MBE	Molecular Beam Epitaxy
ML	Monolayer
NA	Numerical Aperture
NW	Nanowire
μ-PL	Micro-Photoluminescence
SC	Self-Catalyzated
SEM	Scanning Electron Microscopy
SF	Stacking Fault
TEM	Transmission Electron Microscopy
VLS	Vapour-Liquid-Solid
WF	Wave Function
WZ	Wurtzite
ZB	Zincblende

Contents

Chapter 1

Introduction

Nanotechnology is the fabrication and characterization of devices and structures with feature size less than 100 nm [1]. As quantum mechanical effects becomes more dominant as the size decreases, nanoscale materials have been found to behave differently than their bulk form [2]. This makes nanomaterials a promising candidate for improving device performance including size reduction as well as cost reduction. Today, nanotechnology has shown the potential to influence many sciences and technologies, making an impact in areas like medical care, energy storage and consumer electronics.

The properties and synthesis of semiconductor nanowires (NWs) have increased greatly in interest in the last few years. Properties such as small device size, relaxation of lattice matching requirements and vast possibilities for bandgap engineering render NWs highly promising for electronic and opto-electronic applications. Indeed, experiments have shown possible future applications in both optically and electrically pumped NW lasers, NW light emitting diodes and NW FET-transistors, to name a few.

The direct bandgap, high electron mobility and easy lattice matching to all other III-V materials make Gallium arsenide (GaAs) a suitable material for implementation in nanoscale media. Though GaAs exhibits zincblende (ZB) crystal structure in bulk, it has been shown to exhibit wurtzite (WZ) crystal structure in gold-assisted molecular beam epitaxy (MBE) grown NWs by the vapour-liquid-solid (VLS) approach. Though this is the primordial technique used to achieve GaAs NWs [3], self-catalyzed (SC) growth by the same growth approach has become well established as well. In contrast, SC growth yields predominantly ZB structure and has the benefit to

be free of gold (Au) which is beneficial for integrating III-V NWs into the well developed platform of silicon (Si) technology. Au is known to be detrimental to the electric properties of Si as it easily diffuses into the material causing midgap defects [3–5]. High quality III-V(GaAs) NWs can be obtained on expensive substrates, hence integration with the cost-effective Si technology is desired [5].

Recent work has shown that ZB GaAs NWs grown by the SC technique may have ultra-high purity and outstanding structural quality [6, 7]. The goal of the project is to characterize SC GaAs NWs with and without AlGaAs shells to help optimize growth conditions in order to raise the quality of SC GaAs NWs to the high quality level of the Au-assisted NWs grown at NTNU. The ambition is to achieve high photoluminescence (PL) brightness of the free exciton emission line at 1.515 eV at low temperature as well as the band-to-band luminescence at 1.425 eV at room temperature. Improved optical quality is of critical importance for implementation of these NWs into devices such as NW solar cells. This thesis deals with PL measurements on SC GaAs NWs grown at NTNU for the first time and will be supporting further work on SC GaAs NWs at the university.

NWs from the same batch may differ greatly in diameter and length as well as composition and occurrence of defects. The NWs selected for this report are picked and studied beforehand by a scanning electron microscope (SEM) to ensure single wire measurements. Experiments have proved SEM imaging not to alter the optical properties of the NWs, while transmission electron microscopy (TEM) performed at 200 kV has been shown to be detrimental [8]. Additional care has to be taken not to damage the NWs in the course of the experiment by high excitation. However all NWs are distributed on TEM grids in order to gain further understanding on the correlation between structure and optical properties by studying the same samples with TEM later on.

Chapter 2

Nanowires

2.1 SC GaAs NWs

GaAs has a stable ZB structure in bulk and thin films where the thin films are known for being single-crystalline. GaAs NWs grown by the SC technique exhibit predominantly this very crystal structure unlike Au-assisted growth which yields predominantly WZ crystal structure. However SC and Au-assisted GaAs NWs may also reveal WZ and ZB phases respectively as well. In this work the MBE growth parameters are optimized to yield ZB SC GaAs NWs and WZ Au-assisted GaAs NWs.

Although Au is the most frequently used seed particle for NW growth, it diffuses easily on and in Si causing detrimental midgap defects [3–5]. However, SC GaAs NWs may be grown directly on Si by MBE thus eliminating the negative effects of using Au as seed particle such as detrimental effects on internal quantum efficiency (IQE) in photosensitive devices [7].

Table 2.1: Sample descriptions.

Sample no.	Comment
A	Undoped
B	Beryllium (Be) doped core
C	Undoped. GaAs core grown relatively slower
D	Undoped
E	Undoped. An axial AlGaAs segment grown before Ga droplet consumation to seperate the WZ segments
F	Be doped core and Si doped shell

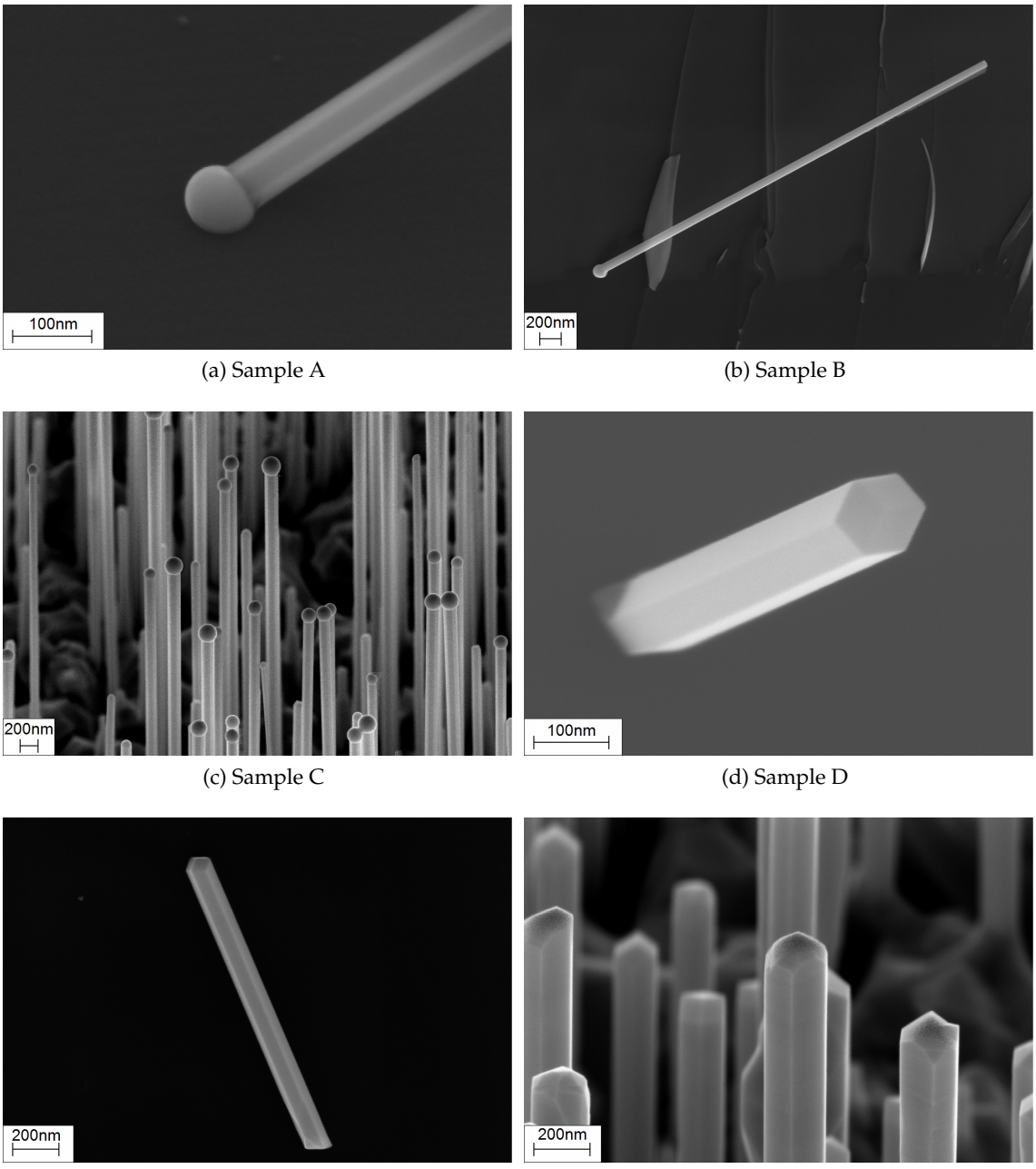

(a) Sample A (b) Sample B

(c) Sample C (d) Sample D

(e) Sample E (f) Sample F

Figure 2.1: SEM micrographs of NWs from the respective samples.

Figure 2.1 presents SEM micrographs of the SC GaAs NWs studied in this thesis, all grown by the SC approach. Sample A through C are SC GaAs core NWs while sample D through F are SC GaAs/AlGaAs core-shell NWs.

A short description of the samples are provided in table 2.1. The tips of the SC GaAs core NWs are all droplet-terminated. Ga droplets are comparably larger than the Au droplets for Au-assisted GaAs NWs which causes a characteristic mushroom shaped tip as can be seen in figure 2.1a-c. The solidified droplet is pure Ga and amorphous. For the core-shell NWs however, the shell is grown after the core is completed. As a consequence, the Ga droplet is either consumed or solidified to avoid axial AlGaAs throughout shell growth. The tip becomes tapered and is therefore the preferential area of deposition of the AlGaAs shell which forms a (110) facet tip, as seen in figure 2.1d-f, during growth. However, WZ segments occur as the Ga droplet solidifies or is consumed. The intention of sample E is therefore to seperate the WZ segments from the main ZB core by growing an axial AlGaAs segment before Ga droplet consumation. Figure 2.2 shows schematic cross-sections of the NWs from the respective samples.

Sample C is grown with a planar growth rate of 0.3 monolayers (MLs) per second for 2 h which is considerably slower than the other samples as can be read in further details in section 3.2. The purpose of this sample is to replicate the excellent PL results obtained by Spirkoska et al. [6]. By growing at a slow planar growth rate on a GaAs(111)B substrate, the group achieved PL peaks with 6 meV full width at half-maximum (FWHM) at 1.15 eV which corresponds well to the free exciton of undoped bulk ZB GaAs. By giving sufficient time to the atoms of the growing material, the anti-site defect density should diminish and thereby perfect stoichiometric ZB GaAs NWs should grow.

The main purpose of growing the AlGaAs shell is to passivate the surface states and avoid Fermi level pinning at the surface. In addition, AlGaAs has a wider bandgap compared to GaAs which ensures that PL will predominantly originate from the GaAs core even if both core and shell are excited. Also, the choice of AlGaAs ensures good lattice match with the GaAs such that strain is not an issue.

2.2 Au-assisted GaAs NWs

Recent work has shown GaAs NWs with WZ crystal structure when grown with Au-assisted MBE, however with an abundance of stacking faults (SFs) and other crystal defects. The WZ phase have been theoretically predicted to have different optical and electronic properties than the ZB phase, among others a different bandgap. A SF in this structure is crystallographically equivalent to a one unit cell thick quantum well of ZB GaAs embedded in

the WZ GaAs continuum.

These SFs form a type II heterojunction with the WZ structures, resulting in a quantum well confining the diffusing electrons at low temperatures. This is explained in further detail in section 4.2. Research shows the NWs to be SF-free upto a certain length above which high density of SFs and other structure defects are formed. Other types of crystal defects than SFs are more extensive, especially closer to the tip where twins and polytype structures occurs frequently as well. The Au-assisted WZ GaAs wires referred to by this thesis are clad by a radially grown shell of AlGaAs.

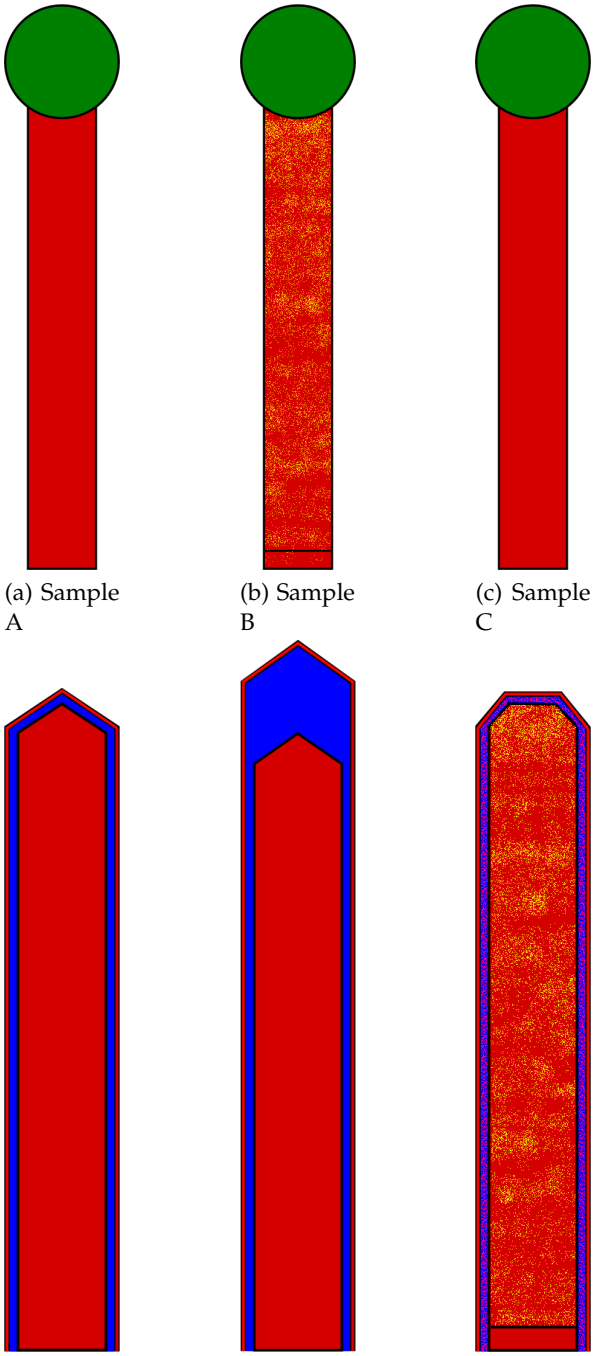

(a) Sample A (b) Sample B (c) Sample C

(d) Sample D (e) Sample E (f) Sample F

Figure 2.2: Cross-section figures of the wires for each sample. GaAs is shown in red and AlGaAs in blue. Ga is shown in green, Be in yellow and Si in pink.

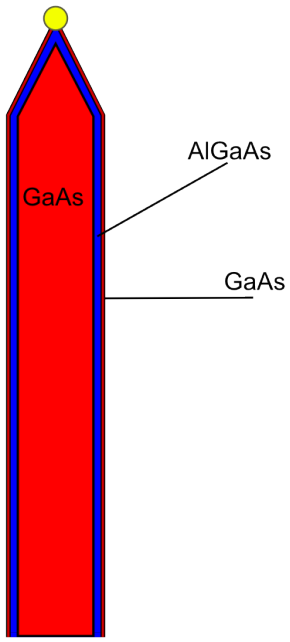

Figure 2.3: Cross section of a Au-assisted WZ GaAs NW. The Au-assisted NWs have a pencil shaped tip as a result of decreasing Au droplet size during the end stage of growth.

Chapter 3

Growth of NWs

3.1 Molecular beam epitaxy

A popular method of NW synthesis is MBE, which is known to be the technique yielding the highest purity materials today. The ability to grow high purity epitaxial films with ML precision makes MBE an attractive choice for device growth [9]. An MBE system normally consists of three vacuum chambers: the growth chamber, the buffer chamber and the load lock. The load lock brings the sample in and out of the system while the buffer chamber is used for preparation and acts as a storage of samples. The growth chamber, where the growth takes place, is pumped down to high or ultra high vacuum to optimize the conditions. The sample substrate is then exposed to a flux of gaseous Ga and As condensing on the wafer. High vacuum is important as the deposition rate is very slow, thus allowing the films and structures to grow epitaxially.

3.2 Self-catalyzed GaAs Nanowires

The bottom-up approach, also named vapour-liquid-solid mechanism, of growing NWs was first demonstrated by Wagner and Ellis in 1964 [10]. The SC growth technique is shown step-by-step in figure 3.1 where the VLS mechanism is presented. As the name suggests, the SC technique utilizes no external metal catalyst for nucleation and growth of the NWs.

A total of six samples, sample A - F, were grown with individually dis-

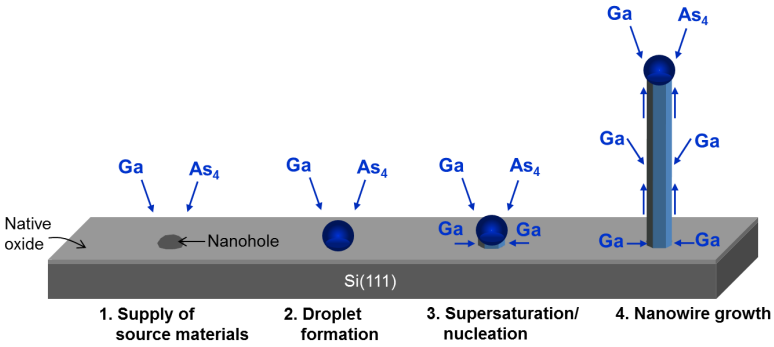

Figure 3.1: GaAs NWs grown by the VLS technique. When Ga and As gas is introduced, GaAs start depositing in the nanoholes on the substrate. Diffusing Ga atoms supports the forming of a droplet which becomes supersaturated. The result is GaAs formation at the interface of the droplet which makes the NW grow.

tinctive parameters, that is growth rate, growth time and doping concentration. Three samples were grown as a single GaAs core NW, known as sample A - C, while three were grown with an AlGaAs shell which are named sample D - F.

p-Si(111) substrates were used for growing the SC NWs. To remove the native oxide the substrates were etched in HF (5%) for 5 sec then rinsed in deionized water for 1 min and dried by blowing nitrogen. The samples were stored in nitrogen atmosphere and after two weeks loaded inside the MBE chamber.

The NW synthesis is carried out at a temperature of $620°C - 640°C$ and grown for 25 min - 2 h depending on the sample. Both As and Ga shutters are opened simultaneously to nucleate and grow the NWs. It is shown that Ga droplets can only form or be maintained in oxide-free openings, hence the Ga adatoms diffuses to the openings from the neighbouring surface supporting NW growth. The surrounding As vapour decompose into As atoms as the molecules impinge on the Ga droplet, diffusing through the droplet alloying with the Ga at the interface of the NW.

Out of the six samples, B and F are p-GaAs core and p-GaAs core with n-AlGaAs shell, respectively. Be was used as p-type and Si was used as n-type dopants. Be is extensively used p-dopant in III-V materials as GaAs and AlGaAs when using MBE. Be has several advantages compared to contenders like zinc and magnesium. It has a lower vapour pressure and a smaller diffusion coefficient which makes controlled growth of doping pro-

files easier to manage [11]. The dopant for the AlGaAs shell is chosen to be Si as it acts as an n-dopant with it's extra electron in the outer shell. In theory however, Si is amphoteric incorporated in III-V compounds, but is, depending on the growth conditions, an n-dopant. The p-doped core and n-doped shell make up a pn-junction which is an elementary part of solar cells, the latter being one of the main outlooks of NW PL characterization.

3.2.1 Zincblende GaAs core Nanowires

Sample A was grown for 25 min by opening the shutters at the same time and closing them accordingly afterwards. The growth of Sample B was initiated by opening the Ga and As shutters simultaneously and the Be shutter 10 sec after. The Be cell temperature was set to $990^{\circ}C$ which gives a nominal p-type doping concentration of $3 * 10^{18}/\text{cm}^3$ on planar GaAs(100). NW growth was done for a duration of 40 min and like sample A the growth was stopped by closing all the shutters and at the same time ramping down the substrate to room temperature.

Sample C is grown much slower than the previous wires with a planar growth rate of 0.3 ML/s for 2 h. Also, the As flux is $2.8 * 10^{-6}$ Torr which is relatively lower pressure.

All parameters are presented in table 3.1 below.

Table 3.1: ZB GaAs core NWs growth parameters.

Parameters	Sample A	Sample B	Sample C
GaAs Planar growth rate	0.7 ML/s	0.7 ML/s	0.3 ML/s
Growth time	25 min	40 min	2 h
Growth temperature	$620^{\circ}C$	$640^{\circ}C$	$620^{\circ}C$
As flux	$4.2 * 10^{-6}$ Torr	$5.5 * 10^{-6}$ Torr	$2.8 * 10^{-6}$ Torr
Doping concentration	0	$3 * 10^{18}/\text{cm}^3$	0

3.2.2 Zincblende GaAs/AlGaAs core-shell Nanowires

For the first core-shell NW sample, Sample D, the GaAs core was grown for 25 min after which the Ga shutter was closed for 10 min and the As flux increased to $1.0 * 10^{-5}$ Torr in order to consume the Ga droplet into the NW material. The AlGaAs growth was then initiated by opening Ga and Al shutters for 15 min. Finally, a GaAs cap was grown for 4 min to prevent

oxidation of the AlGaAs shell. Sample E shares the same growth procedure as Sample D with the exception of an axial AlGaAs segment grown 1 min just before Ga droplet solidification. Sample F is Be doped p-GaAs core and Si doped n-AlGaAs shell NWs. The core was grown in the same way as sample B and the Ga droplet was solidified by increasing the As flux to avoid axial AlGaAs growth at the shell growth stage. The substrate temperature was then reduced to $540^{\circ}C$ in order to grow the Si doped AlGaAs shell. The shell growth was carried out for a duration of 20 min followed by an 8 min growth of a Si doped GaAs cap. The Si cell temperature was set to $1295^{\circ}C$ which would produce a nominal n-type doping concentration of $1 * 10^{18}/\text{cm}^3$ on planar GaAs(100).

All parameters are presented in table 3.2 below.

Table 3.2: ZB GaAs/AlGaAs core-shell NWs growth parameters.

Parameters	Sample D	Sample E	Sample F
Ga Planar growth rate core	0.7 ML/s	0.7 ML/s	0.7 ML/s
Ga Planar growth rate shell	0.7 ML/s	0.7 ML/s	0.4 ML/s
Al Planar growth rate shell	0.3 ML/s	0.3 ML/s	0.2 ML/s
Growth time core	25 min	25 min	40 min
Growth time shell	15 min + 4 min	15 min + 4 min	20 min + 8 min
Growth temperature core	$640^{\circ}C$	$640^{\circ}C$	$620^{\circ}C$
Growth temperature shell	$640^{\circ}C$	$640^{\circ}C$	$540^{\circ}C$
As flux	$5.5 * 10^{-6}$ Torr	$5.5 * 10^{-6}$ Torr	$1.5 * 10^{-5}$ Torr
Doping concentration	0	0	$1 * 10^{18}/\text{cm}^3$

3.3 Au-assisted GaAs Nanowires

Growth of the Au-assisted GaAs NWs differs from the SC GaAs NWs on several factors and parameters. The Ga rich droplet is substituted by a Au particle, the As flux is higher and the growth temperature is lower. The Au-assisted GaAs NWs are grown on a GaAs(111)B substrate which is As terminated. The Au-assisted technique is shown in figure 3.2 below.

Starting with a de-oxidized substrate surface, a 200 nm layer of GaAs was grown in order to achieve an atomically flat surface level. The next main step is the Au layer deposition of a 5 Å thick film followed by annealing with As flux in the MBE growth chamber. The Au particles formed on the substrate acts as a catalyst, resulting in an eutectic with Ga. Consequently, Ga precipitates out at the three-phase particle interface forming GaAs with the surrounding As vapour. As a result, the NWs grow along

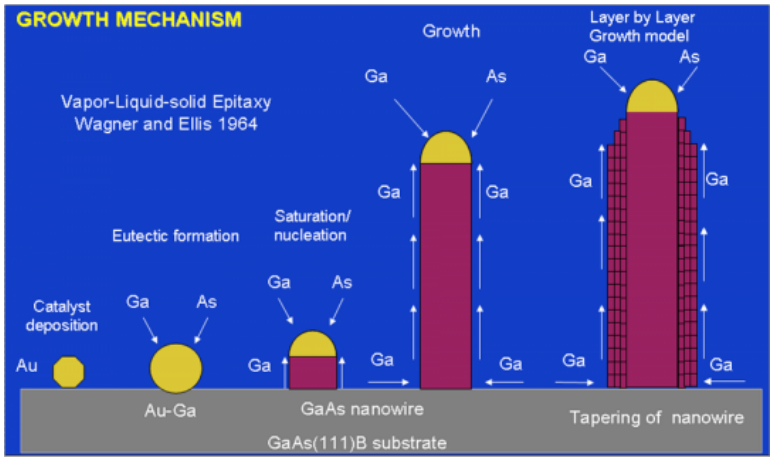

Figure 3.2: GaAs NWs grown by the VLS technique. The Au particle forms a catalytic liquid alloy phase as the As and Ga gas is introduced. As the phase reach supersaturation level, crystal growth occur at the liquid-solid interface hence the one-dimensional growth [9].

the c-axis of the hexagonal unit cell forming a vertical rod. This way of growing is known as *Au-assisted growth* [7] and is the method used for to create the WZ GaAs NWs studied in this report.

Ga starts depositing radially on the wire as the NWs grow higher than the diffusion length of Ga. The growth of the AlGaAs shell is initiated a certain time after opening the shutter of the Ga effusion cell [12]. In fact, Al has lower diffusion length than Ga resulting in uneven concentrations in the shell along the wire.

Chapter 4

Electronic Properties of GaAs NWs

4.1 Band structure

For a single isolated atom, electrons occupy discrete energy levels depending on the distance to the core which are grouped in shells containing a corresponding number of atomic states [13]. In crystals, the electrons in the incomplete outer shells are shared by all the atoms in the crystal. As a large number of atoms are brought together, these valence electrons interact with each other via the quantum mechanical Pauli principle so that their energy levels are spread into quasi-continuous energy bands [14].

Looking at the bands with respect to their energy ranges one recognizes certain important aspects of the solid. The valence band is the highest range of energy where the electrons are normally present at zero Kelvin. On top of it is the conduction band. This is where the electrons contain enough energy to free themselves from bonding and move quasi-freely in the material. The band structures shown in the figure represent three major types of materials; semiconductor, semi-metal and metal. The forbidden band between semiconductors, called the band gap, depicted as E_g in figure 4.1 is of major importance in the field of semiconductors as its width is related to the emission wavelength.

Plotting the energy dispersion relation reveals, among other important electronic properties of the material, whether its band structure is direct or indirect. This is seen by whether the minimum point of the conduction

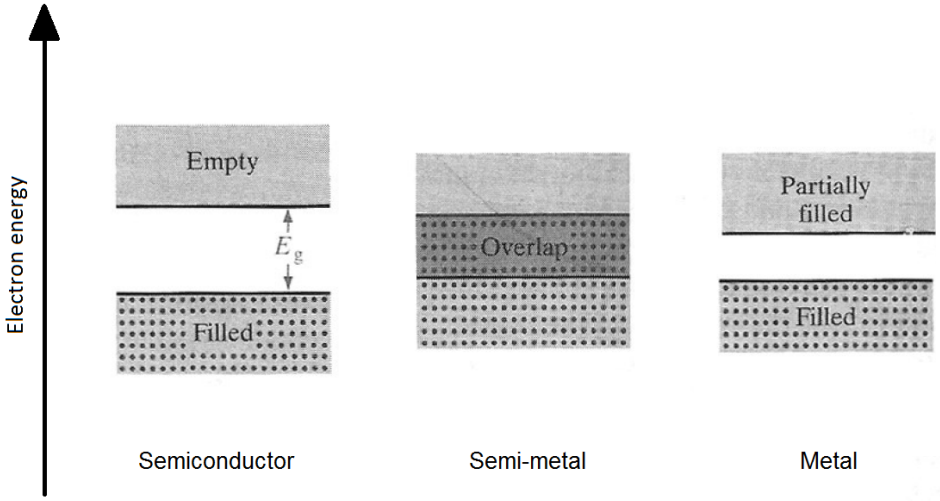

Figure 4.1: Band structure generalization and electron occupation of semiconductors, semi-metals and metals at 0 K.

band and the maximum point of the valence band are aligned to each other. If the lowest energy gap is located at the zero momentum point, which is in the center of the *Brillouin zone*, the band gap is then direct and carriers can recombine radiatively between the conduction and the valence bands.

Figure 4.3 presents the calculated band structure of ZB GaAs by Brozel and Stillman [16]. Both ZB and WZ GaAs have a direct band gap at the Γ point.

4.2 Heterojunctions

Materials with different structure and/or composition joined together form an interface resulting in a dissimilarity in the band alignment known as a heterojunction. The reason for this is that different semiconducting materials commonly have unequal band gaps, electron affinity and work function.

The ternary compound AlGaAs, present in the shell of the WZ GaAs NW and three of the samples of ZB GaAs NWs, has a larger bandgap than GaAs depending on the concentration of aluminium. An interface between GaAs and AlGaAs corresponds to a type I heterojunction seen in figure 4.4. This in turn corresponds to a more probable diffusion of carriers from AlGaAs to GaAs than the other way around due to the energy gap difference.

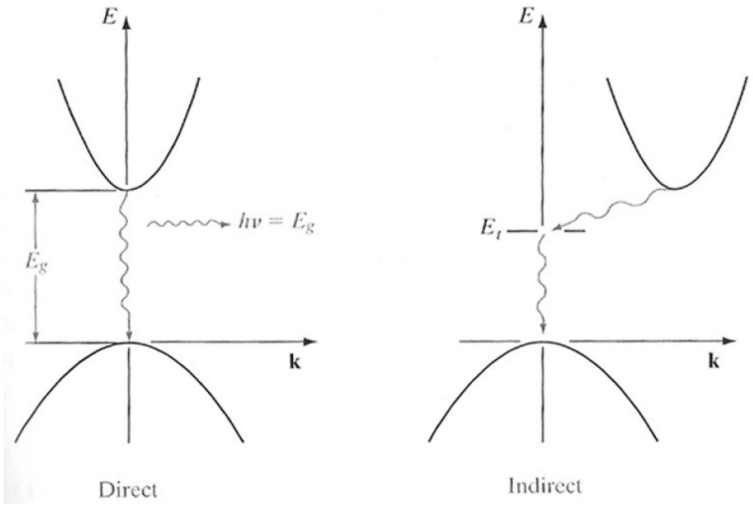

Figure 4.2: General dispersion relation between the conduction band and valence band for direct and indirect band gaps [15].

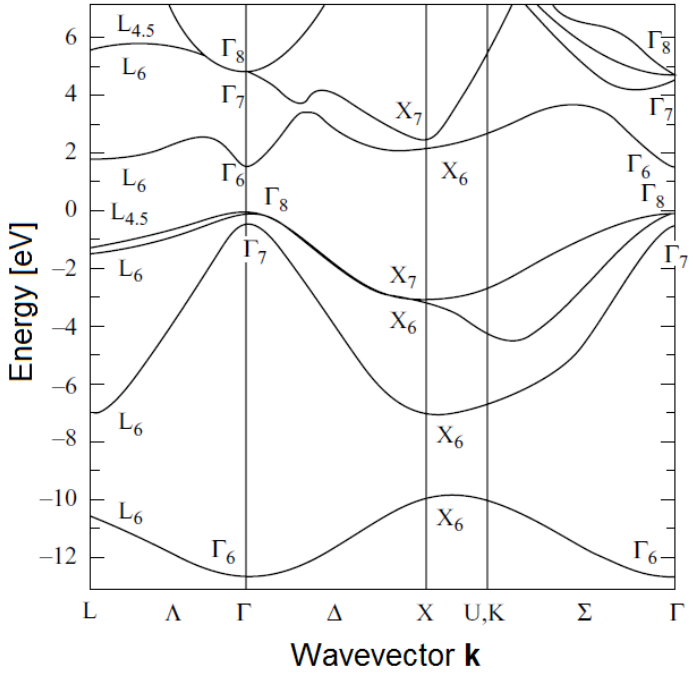

Figure 4.3: Calculated band structure for ZB GaAs [16].

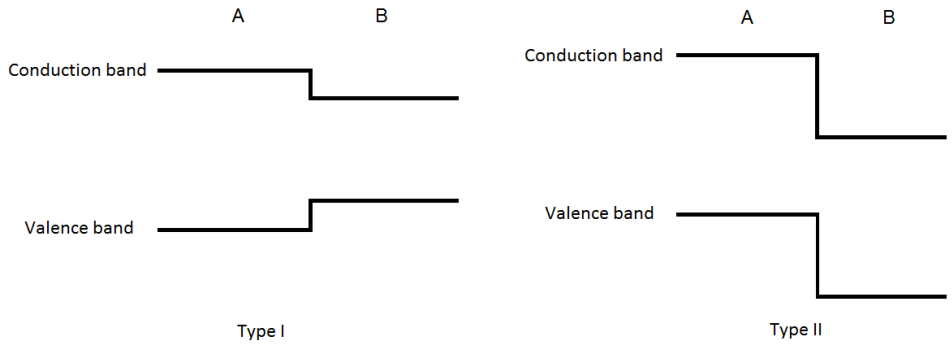

Figure 4.4: Heterojunction type I and type II are both occuring in the NWs grown for this thesis. A and B marks the heterogenous materials.

Unlike the GaAs/AlGaAs interface, ZB and WZ GaAs form a type II homomaterial heterojunction because of the higher electron affinity of the ZB structure and band offsets. As a consequence, the WZ segments occuring near the tip of SC ZB GaAs NWs may trap the holes while acting as barriers for diffusing electrons. This is the heterojunction for SFs in Au-assisted WZ GaAs NWs where the ZB segment thickness is one unit cell. The type II heterojunction is presented in figure 4.5.

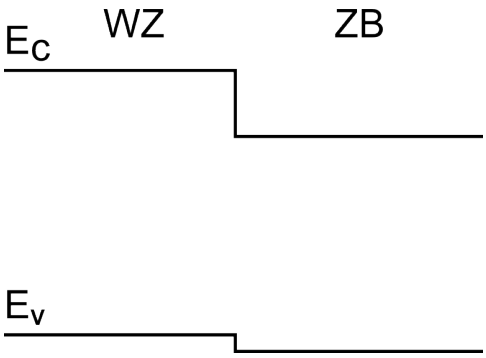

Figure 4.5: A type II heterojunction between WZ and ZB.

4.3 Semiconductor doping

A key property of semiconductors is the fact that their conductivity can be engineered by e.g. doping. In semiconductor fabrication, this is achieved by introduction of impurities into the crystal lattice of the pure, or *intrinsic*, semiconductor as point defects. These impurities acts as donors or acceptors of electrons depending on the valence electrons to be weakly or

strongly bound to the impurity relative to the surrounding lattice atoms. Semiconductors doped with donor impurities are called n-type, whereas acceptor doped semiconductors are known as p-type.

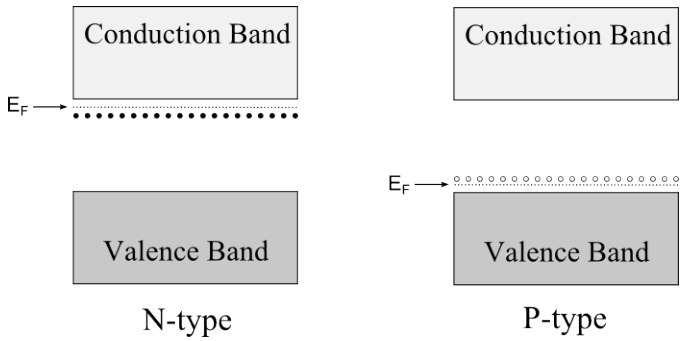

Figure 4.6: In P-type semiconductors, donor impurites create states near the conduction band. However in N-type semiconductors the acceptor impurities create states close to the valence band. The states are represented by dots close to the Fermi level marked as E_F.

Semiconductor doping directly affects the band structure as seen in figure 4.6 where the impurities adds allowed energy states within the bandgap. As a consequence, the Fermi-level shifts to a point between the new energy states and the closer band.

The resulting energy gap between these states and the nearest band becomes significantly smaller than the nominal band gap of the undoped material, thus the number of free charge carriers increases.

Chapter 5

Emission and absorption

5.1 Fermi's golden rule

To get an insight of the optical properties of semiconductors it is important to acquire knowledge of the material's transition rates between states in different bands. When the transition probability is constant in time, it is commonly expressed by *Fermi's golden rule*. The optical transition rate between any two levels i↔j is

$$W_{ij} = \frac{\partial}{\partial t}|C_{ij}^{(1)}|^2 = \frac{2\pi e^2}{\hbar^2}|z_{ij}|^2|E_z|^2\delta(\omega_{ji} - \omega) \tag{5.1}$$

Equation (5.1) is Fermi's golden rule for a single atom. The dipole matrix element $|z_{ij}|^2$ contains the selection rules [17] which determine whether the transition is allowed or forbidden. If $|z_{ij}|^2 = 0$, the transition is forbidden and is otherwise allowed. In ZB GaAs, both parallel and perpendicular polarizations are allowed. The Γ point selection rules are especially important as it is situated where GaAs has a direct bandgap.

However, equation (5.1) considers transitions between either totally occupied or vacant levels. Following Fermi-Dirac statistics for electrons it is noticed that the transition probability is proportional to the number of occupied initial and vacant final states. Instead of single levels, quasi-continuous energy bands have to be considered in a solid. These generalizations leads to the equations below.

$$
\begin{aligned}
W_{v\to c} &= \frac{2\pi e^2}{\hbar^2}|z_{cv}|^2|E_z|^2 D(\omega_g-\omega) f_{FD}(E_v)[1-f_{FD}(E_c)] \\
W_{c\to v} &= \frac{2\pi e^2}{\hbar^2}|z_{vc}|^2|E_z|^2 D(\omega_g-\omega) f_{FD}(E_c)[1-f_{FD}(E_v)]
\end{aligned}
\tag{5.2}
$$

The first and the second equation in (5.2) treats absorption and emission respectively. The two expressions are very similar, the population factors being the only difference between the transition rates.

5.2 Absorption and luminescence

The first equation of (5.2) is absorption, hence $|E_z|$ is the electric field of the excitation light.

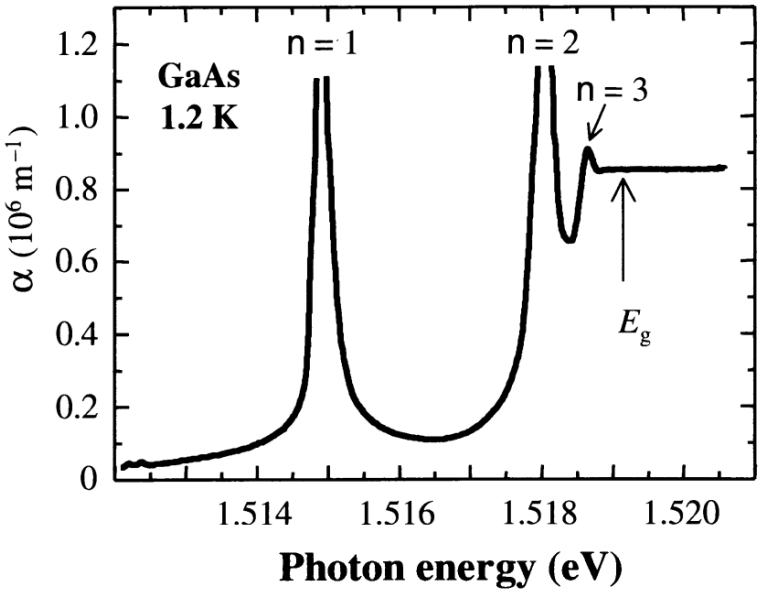

Figure 5.1: The intensity peaks corresponds to excitonic absorption in pure GaAs at 1.2K [18].

At energies larger than the bandgap, the absorption edge is observed. At lower energies, just below the bandgap, several absorption lines could be observed in extremely pure materials corresponding to excitonic absorption. Figure 5.1 shows the excitonic absorption for the first three exciton states noted as 'n'.

Luminescence, meaning emission of light, is fundamental for opto-electronic devices. *Photoluminescence* is the phenomenon used in this report, where the carriers are excited by means of absorption of light from an external source.

When the carriers are excited, they quickly relax to the edge of their band without emitting photons, a process known as thermalization. The excess energy is released through collisions and lattice vibrations. The resulting dense population of carriers at the edge of the band is the reason for sharp emission peaks. The second equation of (5.2) deals with luminescence, but as for the NWs for this report only spontaneous emission is considered.

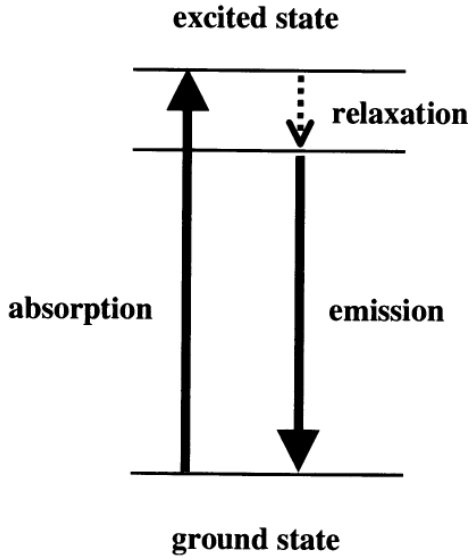

Figure 5.2: The absorption and luminescence process of an atom. When the electron is excited, it may reach several states higher than the ground state. It then relaxes non-radiatively to lower states before eventually recombining radiatively [18].

5.3 Excitons

If an electron from the valence band acquires enough energy to enter the conduction band it will leave a void. This void, or *hole*, is a quasi particle acting and moving similar to electrons, being the mathematical opposite of an electron with opposite charge and different negative effective mass.

The excitation of the electron can be caused by several reasons, with optical absorption as one of the most important. As the charge carriers are generated, they are free to move in their respective bands depending on the kinetic and thermal energy.

The electron is attracted to the hole by the Coulomb force. This bound state acts as a quasi particle called *exciton*, which behaves much like a hydrogen atom [14]. In the case of GaAs, the radius of the exciton is larger than the lattice spacing. This type of exciton is named *Wannier-Mott* excitons and is typically found in semiconductors with narrow band gap and high dielectric constant.

The energy structure of hydrogen-like particles is dependent on the distance between the two components and the medium they are submerged in. For a hydrogen atom this is vacuum whereas for an exciton this is the host semiconductor material with dielectric permittivity larger than unity.

$$E_x = E_g - \frac{E_b}{n^2} + \frac{p^2}{2M} \tag{5.3}$$

The energy of the exciton as shown in equation (5.3) depends on the binding energy of the exciton resulting in a total energy slightly lower than the bandgap. This binding energy, E_B, is found to be 4.3 meV in ZB GaAs but it is not determined in WZ GaAs. The denominator in the second term in equation (5.3) indicates whether the exciton is in its ground state (n=1) or in an excited state (n>1). The last term corresponds to the exciton's kinetic energy.

The exciton relies heavily upon temperature in order to exist. In addition, PL is extremely sensitive to defects to an amount that a low density of defects is able to mask and dominate the free exciton emission. However at low temperatures and when the defect density is negligible, the main light emission is caused by excitons replaced by free electron-hole recombination at higher temperatures where excitons are energetically unfavorable.

When free carriers are generated, they usually recombine shortly after. Radiative recombination occurs only if $k \approx 0$ due to momentum conservation, that is when excitons have relaxed to their ground state and come to a standstill. This would mean that the last term in equation (5.3) approaches zero. Consequently, free excitonic emission corresponds to one discrete line in emission. The exciton, like the hydrogen atom, do not possess metastable states.

Depending on temperature and material purity, excitons may diffuse over large distances through the material. Hence the diffusion length of excitons is greater at lower temperatures. In addition, diffusion length is reduced by scattering at structure interfaces, for instance when moving over a WZ segment or a defect such as a extrinsic atom.

5.4 Non-radiative recombination and defects

Fabrication of NWs leaves the outer layer with dissimilar bonds, so-called *dangling bonds*. The presence of a surface introduces additional energy levels known as *surface states* lying between the valence band and conduction band. In the cases of extremely high density of midgap surface states, the Fermi level becomes pinned at the energy corresponding to that of the midgap surface states [19]. Carriers diffused into these states recombine non-radiatively leaving the position of the Fermi level pinned at the surface-state energy. The ratio of surface area w.r.t. NW volume concludes the surface states to be predominant. This is also the reason why the AlGaAs shell is grown for samples D-F of the SC GaAs NWs as well as all the Au-assisted WZ GaAs NWs.

In ZB GaAs NWs, SFs appear as twins which rotates the facets in the growth direction. However in Au-assisted WZ GaAs NWs they occur as a one unit cell thick ZB segment as mentioned in earlier sections. Native defects, however, can occur in several forms and variations. Indeed, the formation of these defects acutely affects the electrical and optical properties of GaAs [20]. Interstitial defects are atoms occupying a site in the crystal structure differing from the regular lattice pattern. Atoms exchanging positions in the lattice are referred to as anti-site defects. In ZB GaAs NWs, these defects occur as gallium on arsenic place or vice versa. The first occurs predominantly due to the use of Ga as catalyst.

After excitation with a laser pulse, some carriers may become trapped in the WZ and ZB segments where these segments may occur. It follows Schrödinger's equation for a potential well that the particle's probablility density of finding its position, that is the wave function (WF) squared, decays exponentially outside the boundaries of the well. This in turn describes the behaviour of type II heterojunction recombinations where the WFs of the electrons and holes overlap slightly through their exponentially decaying tails. A recombination between the interface is seen in figure 5.3.

When dopants are introduced, absorption and recombination may be

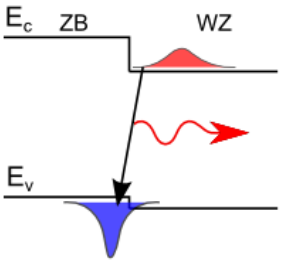

Figure 5.3: Type II band alignment between ZB and a WZ segment. The WFs state a low probability of recombination.

affected in several ways. A simple defect related recombination process is the *free-to-bound* transition where an excited carrier recombine with another carrier trapped at a defect.

Involving two defect centers, electrons and holes may be trapped at donors and acceptors independently and form a pair with interaction energies fixed depending on the distance between the particles. This is known as a donor-acceptor pair (DAP) and is shown together with the free-to-bound transition in figure 5.4.

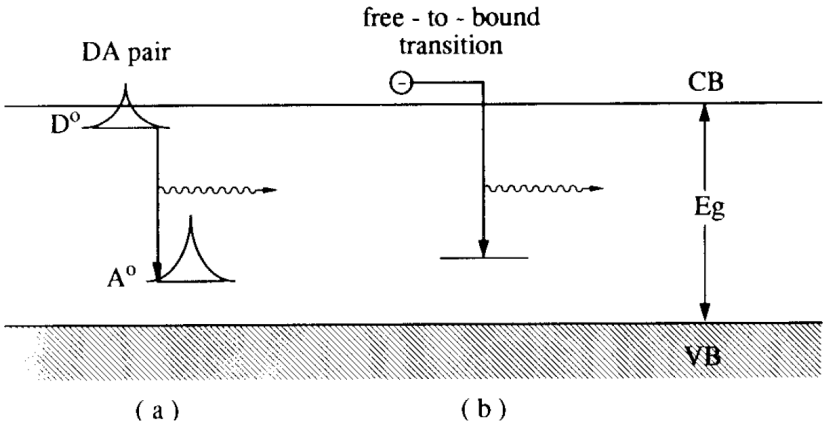

Figure 5.4: (a) DAP transition and (b) free-to-bound transition in relation to the valence and conduction band. the DAP transition involves two defect centers, while the free-to-bound transition is recombination of excited carriers to a defect [21].

Excitons may, similarly to free carriers, be bound to a point defect forming what is known as a bound exciton complex (BEC). Depending on the density of the point defects, the recombining excitons will emit light characteristic to the impurity type. If the density is too big there may be carrier trapping such as DAP or free-to-bound emission. The binding energy of

the BEC depends on the binding energy of the defect as well as the chemical nature of the complex and on the surroundings. Nonetheless, the BEC has normally a larger binding energy than the exciton.

In summary, defect-mediated transitions, as well as heterojunction transitions, introduces luminescence with energy lower than the bandgap. Depending on the occurence of the defects and heterojunctions, these may be seen and identified on PL spectras.

5.5 High excitation effects

The behaviour of electrons and holes in a semiconductor sample depends profoundly on temperature and excitation level. At low temperature and excitation level, single electron-hole pairs determine the optical properties as excitons or in the continuum.

If the sample is pumped sufficiently, the carrier density increases with subsequent scattering processes between the carriers. This may lead to collision-broadening of exciton resonances and to new luminescence bands in the PL spectra. Pumping the sample futher leads the material, or at least parts of the excited volume, to a high density regime of a new collective phase of electron and holes known as electron hole plasma (EHP) [21]. This describes a carrier state where the average distance is comparable to or smaller than their exciton Bohr radius.

When the EHP density increases, the bandgap energy decreases monotonically as a result of exchange and correlation effects, this ultimately leads to a red shift in the PL spectra. This correlation can be explained by the Pauli principle which states that two electrons/holes with parallel spin are forbidden from staying in the same unit cell. This excludes the possibility of random distribution of carriers. The exchange energy thus increases the average distance between electrons/holes with parallel spin, hence the total repulsive Coulomb energy, and hence the total energy of the system, is reduced. The EHP may lower its energy further if there is a higher probability of finding an electron in the vicinity of a hole and vice versa. This occurrence is due to the correlation energy which is spin independent and is the reason of exciton formation at low densities. Experiments on covalently bound semiconductors like GaAs show this bandgap renormalization to be almost independent of temperature [21].

Another important high excitation effect is the result of *Burstein-Moss*

effect, that is when the apparent bandgap is expanding as the absorption edge increases to higher energies due to all the states close to the conduction band being populated. This effect is commonly observed in degenerate semiconductors, namely semiconductors with a sufficiently high level of doping to behave more similar to a metal than a semiconductor. As the doping is increased, for n-type semiconductors the donor states density increases which pushes the Fermi level higher and, in the case of degenerate doping, into the conduction band above the occupied donor states. The same argument holds for p-type semiconductors for the acceptor states. An increase in the measured bandgap is therefore observed as Pauli's exclusion principle forbids excitation to the occupied donor states. The resulting shift in emission energy is also known as a Burstein-Moss shift.

5.6 PL Lineshape

Acquiring a mathematical fit of the PL lineshape is important in order to determine the position of the signal peak excluding the noise. The Lorentz and Gauss lineshape is occasionally used for to fit PL spectra in the field of semiconductors [22]. The Gaussian fit accounts for localization effects and homogeneous broadening.

The atomic energy levels of an atom have a lifetime τ, which is the inverse of the rate at which its population decays to all lower levels, radiatively or non-radiatively. Hence, short lifetimes corresponds to high rates of transition. For the purpose of this report, the rate of spontaneous recombination may be viewed on in terms of a damped harmonic oscillator which generates an exponentially decaying harmonic function $e^{-t/2\tau}e^{j2\pi v_0 t}$ [23]. Following this model reveals the FWHM to be

$$\triangle v = \frac{1}{2\pi\tau} = \frac{1}{2\pi}(\frac{1}{\tau_1} + \frac{1}{\tau_2}) \tag{5.4}$$

Where τ is the transition lifetime between two levels [23]. Thus, by knowing the center frequency from the energy difference between the two layers to be $v_0 = (E_2 - E_1)/h$, the lineshape function is recognized to be of a Lorentzian profile, seen in equation (5.5) below.

$$g(v) = \frac{\triangle v/2\pi}{(v - v_0)^2 + (\triangle v/2)^2} \tag{5.5}$$

Figure 5.5 illustrates the relation between the randomly occuring wavepackets and the resulting Lorentzian lineshape.

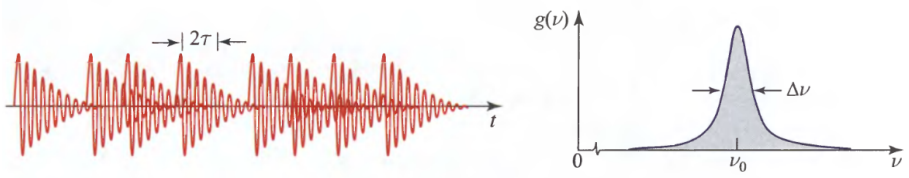

Figure 5.5: Wavepackets occuring randomly with transition lifetime τ. The result is partial coherent light with spectral intensity depicted by the Lorentzian function with FWHM to the right [23].

A program code written for the numerical computing program MATLAB [24] was developed in order to acquire lineshape fits for each individual spectrum with a Lorentzian function and a Gaussian function together.

5.7 The Varshni equation

In a paper from 1967, Y.P. Varshni proposed a relation of the energy bandgap, E_g, with temperature T in semiconductors such as GaAs [25]. The relation was invented empirically and was later modified to equation (5.6) below. The equation presents the bandgap as a function of temperature where α, measured in eV/K, and β, measured in K^3, are constants [26].

$$E_g = E_g(0) - \frac{\alpha T^4}{T^3 + \beta} \tag{5.6}$$

The modified Varshni Eq is invented to describe the variation of the energy gap both at low temperatures where it reaches saturation, and at high temperatures where it is linear. Equation (5.6) will be used throughout the text to describe the temperature variation of the emission energy of the SC GaAs NWs studied in this thesis and compare them with experimental data for Au-assisted GaAs NWs and literature data for bulk GaAs.

Chapter 6

Optical setup

6.1 General layout

The general layout of the optical set up is shown in figure 6.1. The photo is taken at the nanophotonics lab in El-bygget at NTNU. This is where all the PL experiments were executed using the equipment shown in the following sections of the chapter. A helium (He) tank shown in the background was moved into the lab at the start of the experiment and connected to the cryostat. The vacuum and He exhaust pump are not shown in this picture. Figure 6.2 displays the beam path from the laser to the sample and the detection path for the PL signal. To make the beam monochromatic, the beam passed through a home-built monochromator (not shown) consisting of a grating, two lenses and a pinhole at their common focal plane. The noise peak present at approximately 810nm from the laser was removed by the set up.

6.2 Lasers and excitation

A Spectra-Physics Millennia^{TM} Pro s-Series diode-pumped, frequency-doubled continuous wave (CW) visible laser [27] was used for all measurements for this report. Operating at the green wavelength of 532 nm, the laser is capable of providing up to 6 W of laser power. The pumping LED array is kept at a stable temperature of 18$^{\circ}C$ by a chiller. A photo of the laser is shown in figure 6.3.

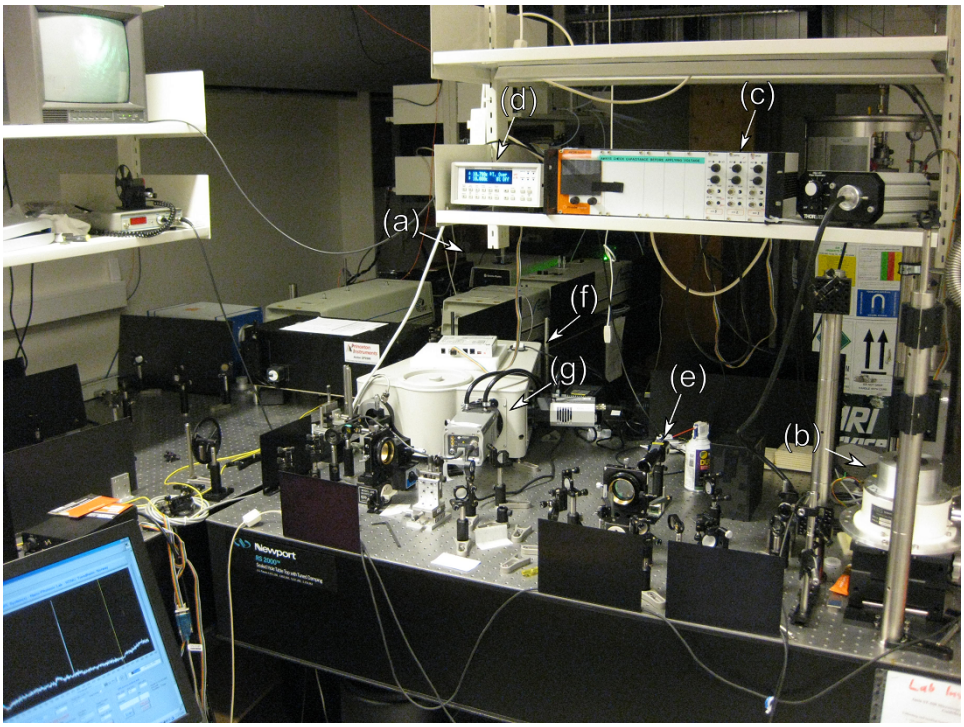

Figure 6.1: A digital camera photo of the PL setup used in the experiments where the devices are indicated by letters. (a) The laser emits light through an optical system to a cryostat (b) which is controlled by a piezo-driven sample positioner (c). The cryostat temperature is supervised on the temperature monitor (d). If necessary, the reflected light may be guided into a camera (e) which displays the sample with or without the laser beam on the TV shown in the upper corner. From the cryostat the light is directed into the spectrometer (f) and lastly into the CCD (g).

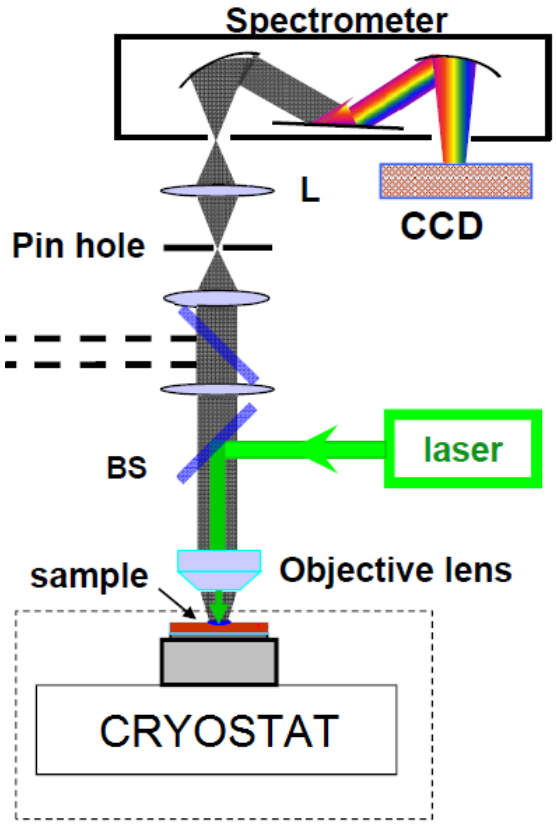

Figure 6.2: A schematic of a spectrometer showing the beam path starting from the laser and ending in the CCD. The dashed line marks the exit to the camera for the TV.

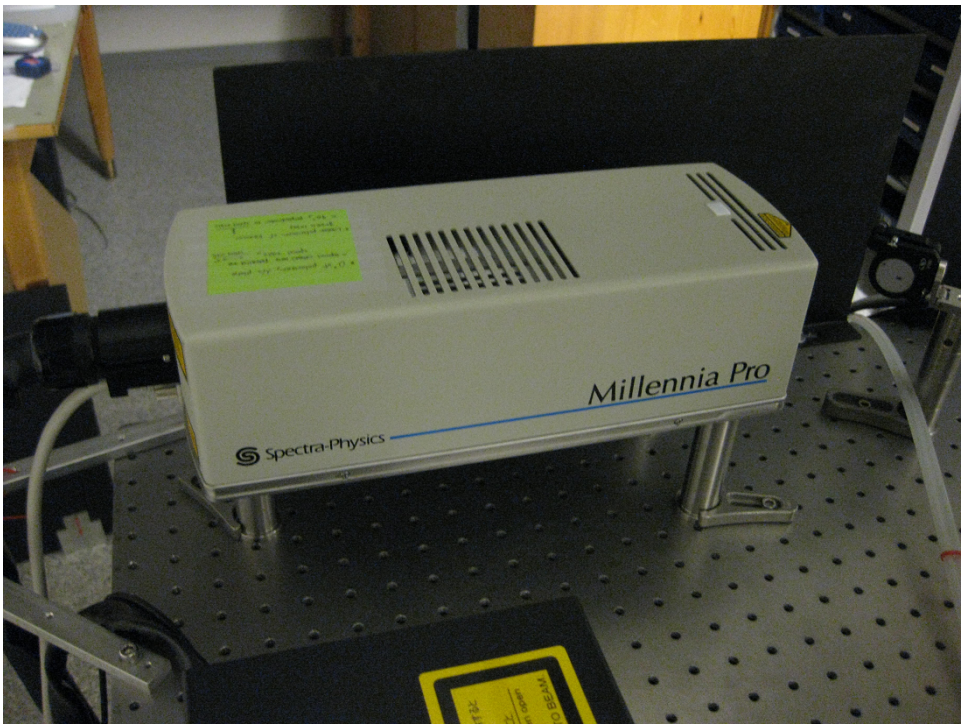

Figure 6.3: A digital photo of the Millennia Pro s-Series laser used for the PL experiments in this thesis.

The laser maintained an output power of 0.23 W during its use. Several grey filters were used to adjust the laser power as monitored at the back-aperture of the lens at the desired level.

The NWs were all excited at 532 nm, corresponding to photon energy well above bandgap. High photon energy provides for more efficient excitation of the NW because the number of possible transitions is increased. The beam spot diameter is approximately 1.5 μm^2.

6.3 Cryostat and sample mounting

The cryostat used in this project was a Janis ST-500 shown in figure 6.4. It is a continuous flow optical cryostat able to perform experiments in the used range of 4 to 290 K. The cryostat has a built-in piezo-driven sample positioner using a long working distance lens placed outside its volume, at room temperature [28]. The lens is a Mitutoyo infinity-corrected and near infrared optimized lens. It has a numerical aperture (NA) of 0.65 and a magnification of 50x. This configuration is highly beneficial for the resolution of the optical system.

In this experiment, liquid helium was continuously transferred through a high efficiency superinsulated line to a copper sample mount, *the cold finger*, inside the chamber where the sample is mounted. A needle valve is present in the transfer line to regulate the cryogenic flow to the cold finger. A thermometer is attached to the cold finger. Figure 6.5 shows a cross section of the Janis cryostat.

The sample was attached to the cold finger with silver paste to ensure high thermal conductivity before evacuating the chamber. When the desired pressure of approximately $5 \cdot 10^{-5}$ mbar was reached, the liquid helium flow was set to cool down the cryostat to obtain the desired temperature. A heater ring inside the chamber was used to regulate the temperature correspondingly to the desired temperature controlled by the temperature monitor displayed in figure 6.1.

6.4 Spectrometer

The Horiba Jobin Yvon iHR500 spectrometer [29] was used to disperse the PL signal from the NWs. A reflection grating spatially distributes the

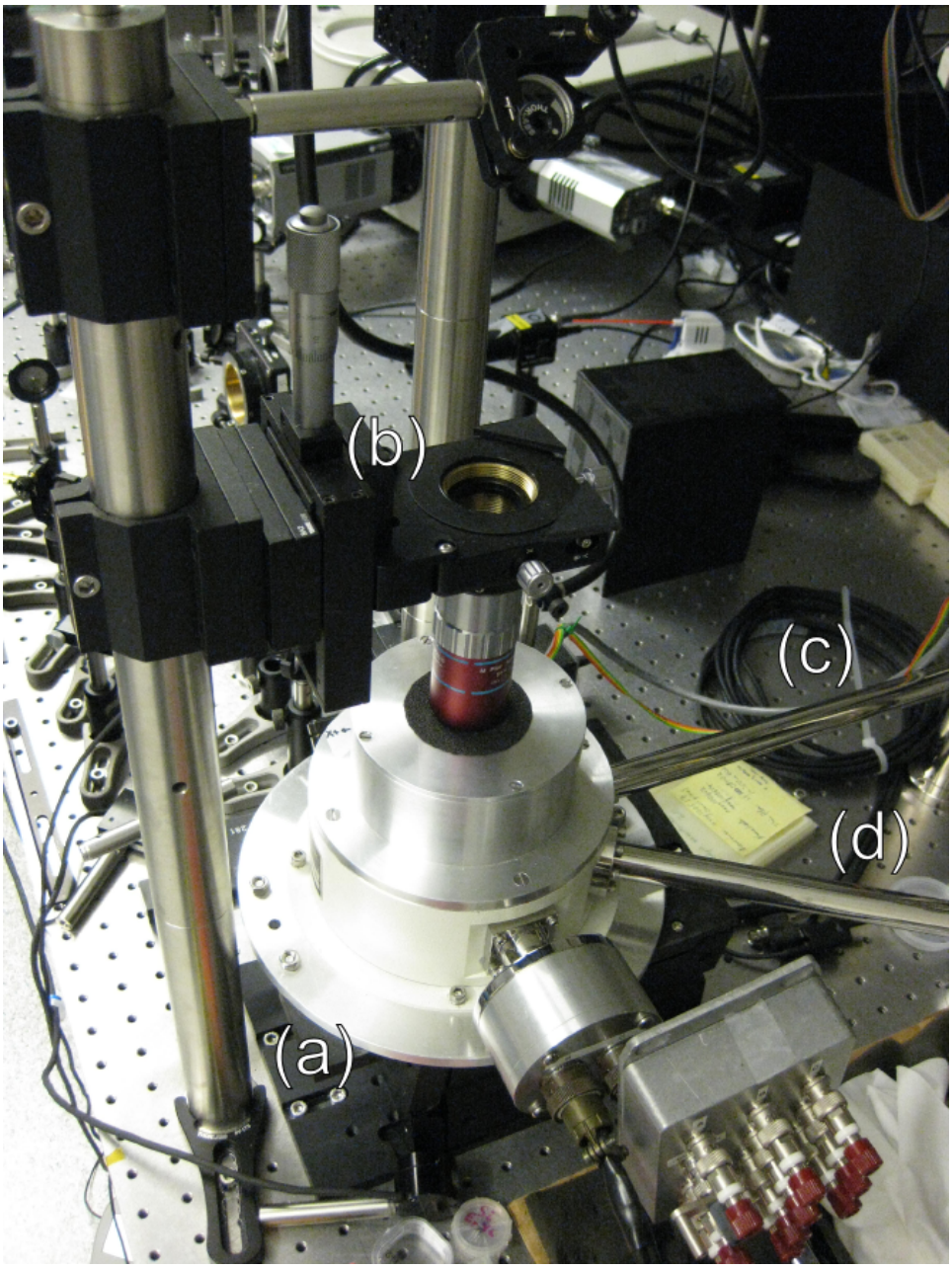

Figure 6.4: A digital photo of the Janis cryostat (a) in the nanophotonics lab. An optical microscope (b) directs the light onto the sample through the cryostat window. The He enters the cryostat through pipe (c) and exits through exhaust pipe (d).

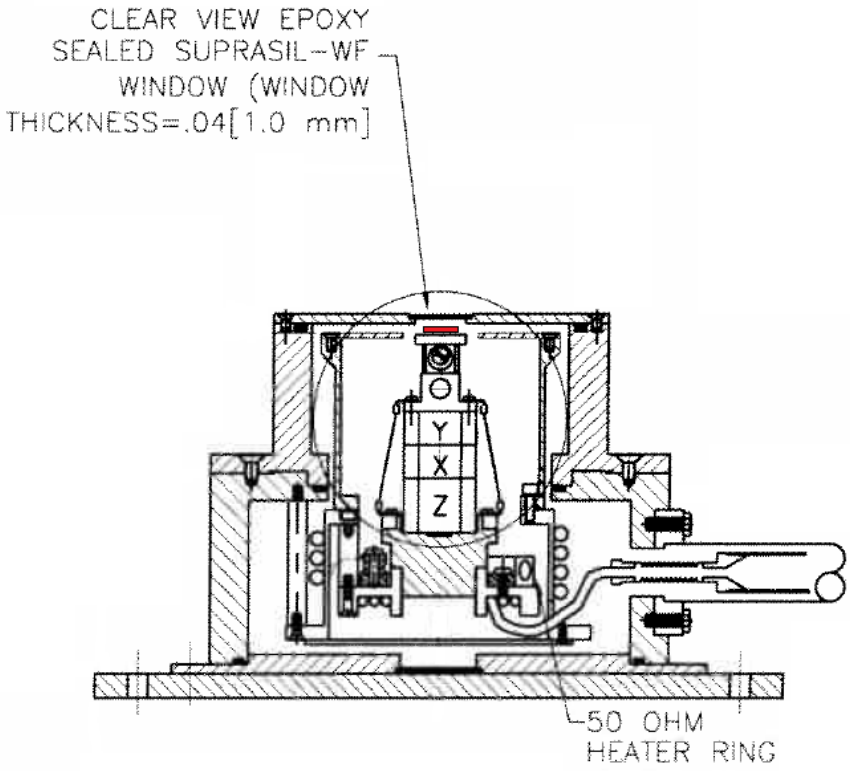

Figure 6.5: A cross-section sketch of the cryostat from the Janis manual. Shown as a red box is the sample mounted on the cold finger. The sample positioner is diplayed with its respective segment directions below the cold finger.

photons according to their wavelength. The signal is then routed to the Charge-Coupled Device (CCD). The spectrometer and camera are utilized by the Laboratory Virtual Instrumentation Engineering Workbench (LabVIEW) software interface. Figure 6.2 displays the beam path where the laser enters the cryostat and into the spectrometer followed by the CCD. A photo of the spectrometer and CCD is shown in figure 6.6.

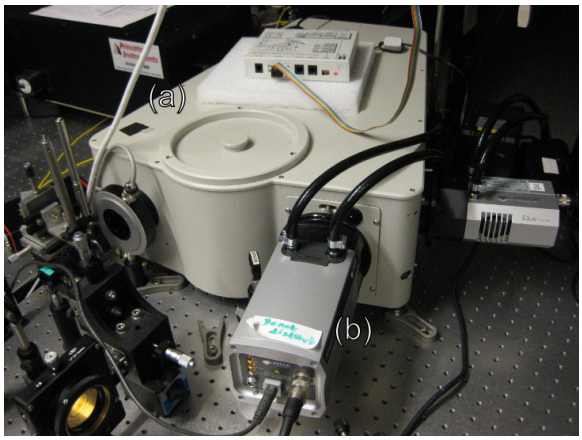

Figure 6.6: A digital photo of (a) the spectrometer and (b) the CCD.

6.5 CCD

The CCD is an Andor Newton^{EM} EMCCD (Electron Multiplying CCD) featuring low noise electronics, 95% QE, multi-MHz readout and cooling to $-100^{\circ}C$ [30]. A photo of the CCD is shown in figure 6.6. The system is optimized for spectroscopic applications with sensors for ultra-low light level applications. It is equipped by a 1600 x 200 pixel array and controlled by the same software interface as the spectrometer.

Chapter 7

Results

NWs for each sample were drop-cast on Si_3N_4 TEM substrates with a thickness of 20 nm or 50 nm [26]. SEM measurements were carried out in order to survey the abundance of single NWs. These were marked on overview images for PL analysis.

For each sample 5-16 NWs were chosen at for measurements at low temperature (10 K) to assure statistically representative results. 3-7 NWs were chosen for further analysis depending on spectral features and the PL brightness of the sample. A set of 4-9 spectra with different excitation powers powers were acquired for each temperature which ranged from 9.6 - 24.6 K (low temperature) up to a maximum of room temperature, that is 294 K.

The NWs were located by monitoring the sample surface while comparing with the SEM images taken beforehand and supervising the position of the laser spot on the sample on a TV screen. Due to setup instability when changing the sample temperature, the setup needed to be realigned at every temperature step. As a consequence, PL intensities at different temperatures are not precisely comparable.

Six NWs were chosen from the PL analysis as representative wires from their respective samples. One or two NWs are chosen from each sample except samples A and C. The selected NWs are listed in table 7.1 with assigned names and the number of peaks appearing at low temperature PL.

Table 7.1: The selected NWs from the radiatively emitting samples with names corresponding to the sample letter. The number of peaks stated in this table are appearing at low temperature PL.

Sample	NW name	Number of peaks
B	B1	2
	B2	1
D	D1	4
	D2	1
E	E1	2
F	F1	1

7.1 Emission spectra at low temperature

In this section, low temperature emission spectra at low excitation powers are presented. The excitation power density of 141 W/cm^2 is chosen to compare the peak emission energies as all NWs were excited with this power density at low temperature. In addition, the FWHM has been calculated for the spectra at this very power density. The NWs are chosen from table 7.1 by a preferable single peak emission.

7.1.1 SC GaAs core NWs

For the SC GaAs core NWs only sample B showed detectable PL signals. For this sample, NW B2 is chosen as the representative NW with single peak emission. Figure 7.1 shows the low power PL of NW B2 at low temperature. The peak emission blue-shift is quite evident looking at the figure. However, at an excitation power of 70.5 W/cm^{2}and higher the peak becomes more consistent.

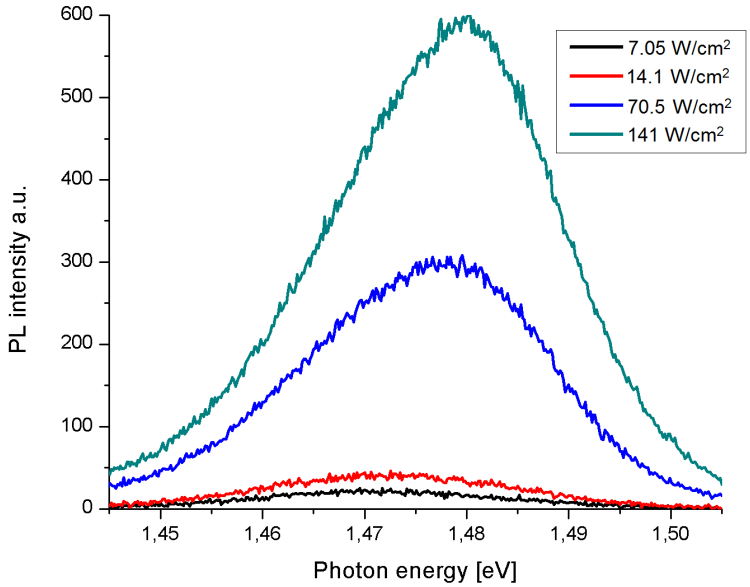

Figure 7.1: Low power PL of NW B2 at low temperature.

The data obtained from the spectra is summarized in table 7.2 where the calculated FWHM value of 26.5 meV is introduced together with the peak emission energy.

Table 7.2: Peak emission energy and FWHM for NW B2 at the excitation energy of 141 W/cm^{2}for low temperature.

NW name	Emission peak	FWHM	Temperature
B2	1.480 eV	26.5 meV	10 K

7.1.2 SC GaAs/AlGaAs core-shell NWs

Unlike the GaAs core NWs there were several NWs from all the core-shell samples emitting distinct PL peaks. One representative NW from each sample, preferably with a single emission peak, are presented here.

Figure 7.2 presents the low temperature emission sepctra of low excitation powers.

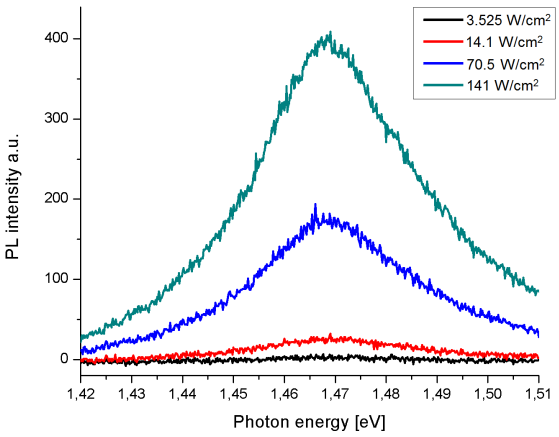

(a) Low power PL of NW D2 at 24.6 K.

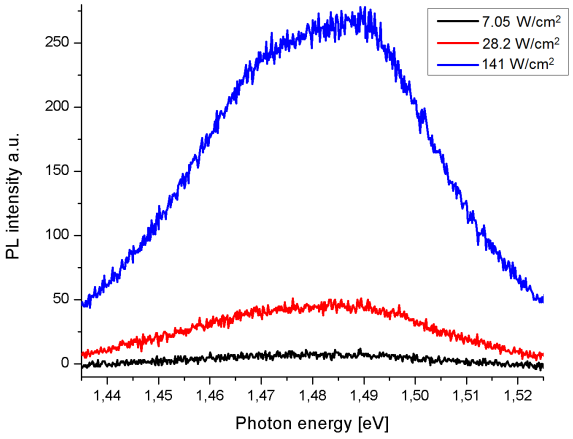

(b) Low power PL of NW E1 at 10 K.

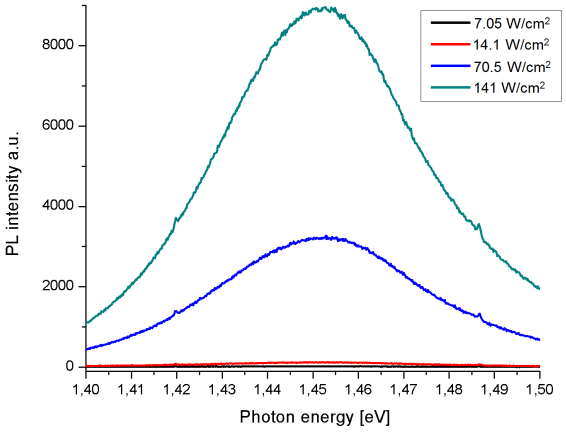

(c) Low power PL of NW F1 at 10 K.

Figure 7.2: Low power PL spectra of NW D2, E1 and F1 at low temperatures. The intensity spikes at ∼1.42 eV and 1.486 eV for NW F1 is caused by laser beam reflections and is not emitted from the sample.

It is seen from the figure that NW D2 emits at 1.469 eV while NW E1 and F1 emits consistently at 1.489 eV and 1.452 eV at low powers respectively. NW E1 also has a low energy peak emission energy at 1.472 eV. Table 7.3 contains the peak emission energies as well as the calculated FWHM for the corresponding spectra.

Table 7.3: Peak emission energy and FWHM for NW D2, E1 and F1 at the excitation energy of 141 W/cm^{2}for low temperature.

NW name	Emission peak	FWHM	Temperature
D2	1.469 eV	37.4 meV	24.6 K
E1	1.472 eV and 1.489 eV	54.4 meV	10 K
F1	1.452 eV	54.3 meV	10 K

7.2 Power dependence

7.2.1 SC GaAs core NWs

The PL spectra of sample A showed no distinct peaks at room temperature even at excitation levels of 84.6 kW/cm^2. This result was repeated consistently for five NWs.

Two NWs are chosen from Sample B where one exhibits two peaks at low powers and the other has a single peak. The low temperature PL spectra for both NWs, named B1 and B2 respectively, are plotted in figure 7.3 below. For NW B1, both peaks blue-shifts as the excitation power is increased, where the lower energy peak becomes indistinguishable from the main peak above 141 W/cm^2. This blue-shift is observed for NW B2 as well. It is seen by the PL spectra that the lower energy peak dominates in intensity at the lowest powers. At 53 K, this peak decreases in intensity, and by 75 K it is dominated by the main peak. At above 150 K, no wires emitted any distinctive PL.

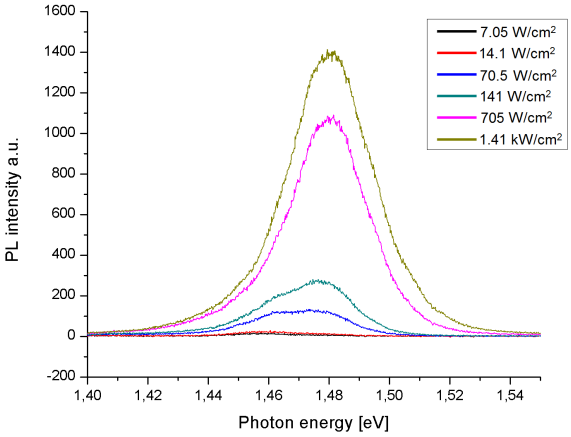

(a) PL of NW B1 at 9.6 K.

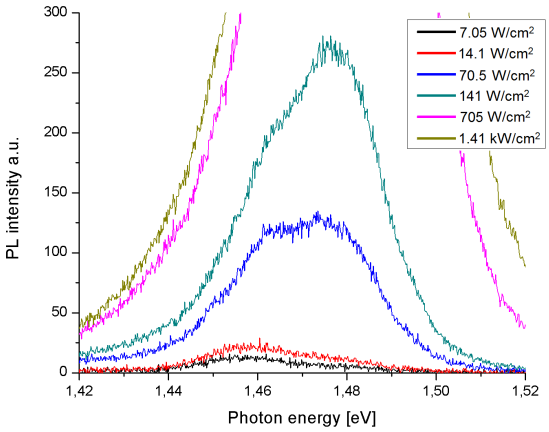

(b) PL of NW B1 at 9.6 K.

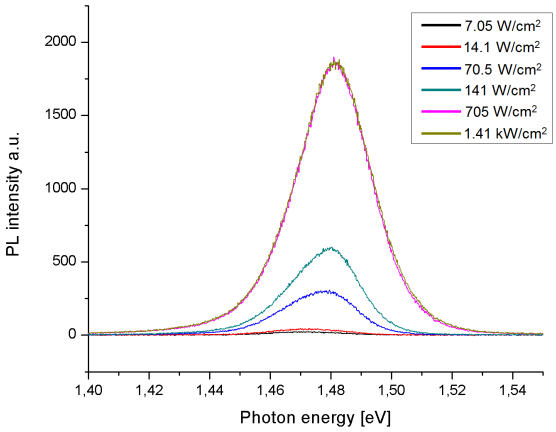

(c) PL of NW B2 at 10 K.

Figure 7.3: PL of NW B1 and NW B2 from sample B. It is clear that NW B1 has two peaks at lower powers in contrast to NW B2.

Table 7.4: Peak emission values for NW B1 and NW B2 at 9.6 K and 10 K respectively.

Excitation power	NW B1 Lower energy peak	Higher energy peak	NW B2 Main peak
7.05 W/cm^2	1.455 eV	N/A	1.472 eV
14.1 W/cm^2	1.456 eV	N/A	1.473 eV
70.5 W/cm^2	1.462 eV	1.476 eV	1.478 eV
141 W/cm^2	1.462 eV	1.476 eV	1.480 eV
705 W/cm^2	N/A	1.482 eV	1.482 eV
1.41 kW/cm^2	N/A	1.482 eV	1.482 eV

A total of 14 different NWs were chosen from sample C at low temperature, however no distinct signal was observed at any power up to 28.2 kW/cm^2.

7.2.2 SC GaAs/AlGaAs core-shell NWs

Similarly to sample B there were two kinds of NWs for sample D, named NW D1 and NW D2 correspondingly, where three out of eleven studied had two peaks while the others exhibited a single peak. The power dependence spectra are plotted in figure 7.4. The PL was seen to be at the highest intensity when exciting at one end of the NWs. The single peak of D2 splits into a second lower energy peak of 1.461 eV at 705 W/cm^{2}excitation power and higher.

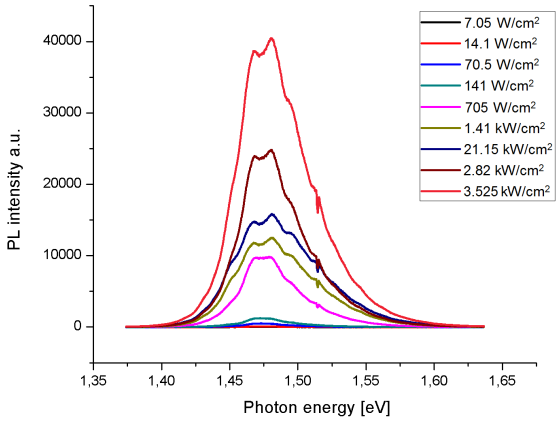

(a) PL of NW D1 at 18 K.

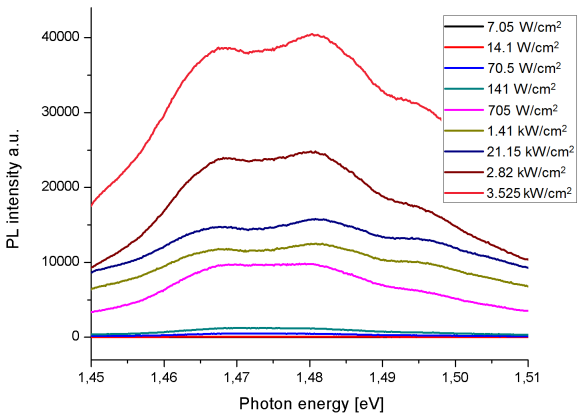

(b) PL of NW D1 at 18 K.

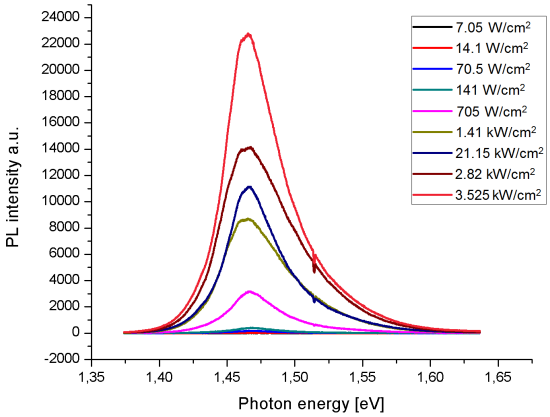

(c) PL of NW D2 at 24.6 K.

Figure 7.4: Power dependence PL of NW D1 and NW D2 from sample D. It is clear that NW D1 has two peaks at lower powers in contrast to NW D2. The intensity drop at ∼1.52 eV is due to a defect on the CCD.

Table 7.5: Peak emission values for NW D1 and D2 at 18 K and 24.6 K respectively.

Excitation power	NW D1 Peak 1	Peak 2	Peak 3	Peak 4	NW D2 Main peak
3.525 W/cm^2	N/A	1.468 eV	1.482 eV	N/A	N/A
14.1 W/cm^2	N/A	1.47 eV	1.48 eV	1.496 eV	1.468 eV
70.5 W/cm^2	N/A	1.47 eV	1.48 eV	1.495 eV	1.468 eV
141 W/cm^2	N/A	1.47 eV	1.479 eV	1.495 eV	1.469 eV
705 W/cm^2	N/A	1.469 eV	1.479 eV	1.495 eV	1.467 eV
1.41 kW/cm^2	N/A	1.469 eV	1.48 eV	1.493 eV	1.466 eV
2.115 kW/cm^2	1.451 eV	1.469 eV	1.48 eV	1.494 eV	1.466 eV
2.82 kW/cm^2	1.451 eV	1.468 eV	1.481 eV	1.494 eV	1.466 eV
3.525 kW/cm^2	1.451 eV	1.468 eV	1.481 eV	1.494 eV	1.467 eV

Power dependence plots of samples E and F are plotted in figure 7.5 and 7.6 respectively. The room temperature emission peak of sample E shifted occasionally when the laser spot was moved and is by that reason not plotted in this section. Two peaks were observed where the main intensity peak was consistently at 1.489 eV and the lower energy peak varied around 1.472 eV when the excitation power was increased. The values are displayed in table 7.6 with the corresponding excitation powers.

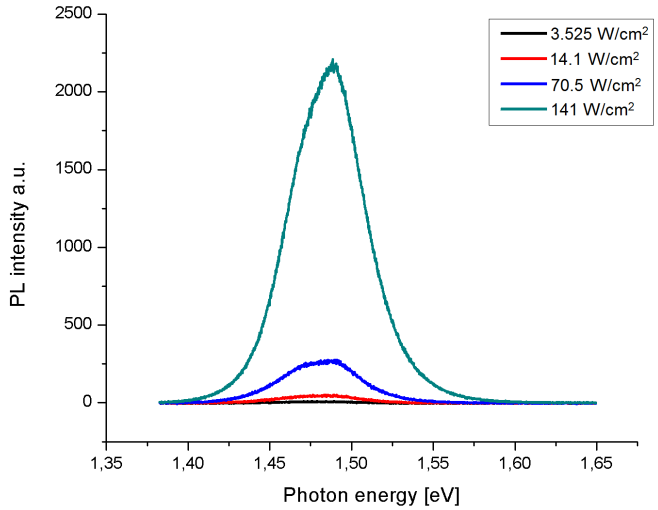

(a) PL of NW E1 at 10 K.

Figure 7.5: Power dependence PL of NW E1 from sample E.

Table 7.6: Peak emission values for NW E1 at low temperature.

Excitation power	10 K Lower energy peak	Higher energy peak
7.05 W/cm^2	1.47 eV	1.489 eV
28.2 W/cm^2	1.473 eV	1.489 eV
141 W/cm^2	1.472 eV	1.489 eV
705 W/cm^2	N/A	1.489 eV

Unlike the previous samples, sample F red-shifts as the excitation power is increased. This effect is observed for all temperatures. The peak emission values from figure 7.6 are presented in table 7.7. The largest red-shift was observed between the excitation powers of 141 W/cm^{2}and 705 W/cm^{2}for all temperatures.

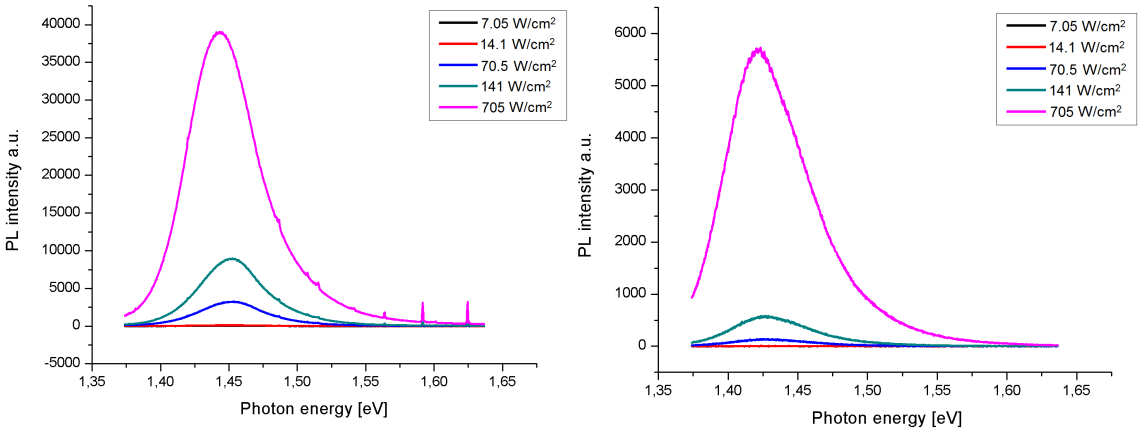

(a) PL of NW F1 at 10 K.

(b) PL of NW F1 at room temperature

Figure 7.6: Power dependence PL of NW F1 from sample F. The small high-energy peaks at low temperature is caused by some reflections by the laser beam.

Table 7.7: Peak emission values for NW F1 at low temperature and room temperature

Excitation power	10 K	Room temperature
7.05 W/cm^2	1.45 eV	1.43 eV
14.1 W/cm^2	1.452 eV	1.43 eV
70.5 W/cm^2	1.452 eV	1.427 eV
141 W/cm^2	1.452 eV	1.427 eV
705 W/cm^2	1.443 eV	1.423 eV

7.3 Temperature dependence

The emission energy for NWs B1, E1 and F1 is plotted in figure 7.7 and fitted with the modified Varshni equation 5.6. The peak energy differ greatly at low temperatures and decreases differently for the different samples as T is increased. NW F1 stand out from the the rest of the NWs as the peak energy abruptly increases at ∼150 K. It is however a representative NW from sample F.

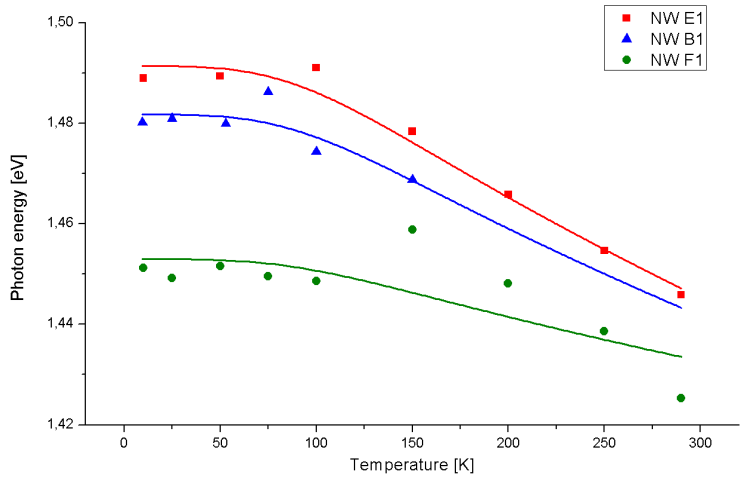

Figure 7.7: Varshni plot of NW B1, E1 and F1. The experimental data is fitted with equation 5.6 represented by the corresponding colored line.

Chapter 8

Discussion

8.1 Emission spectra

To obtain the peak emission energy, low excitation powers must be studied in order to avoid band filling which leads to the Burstein-Moss effect. It is seen from figure 7.1 and 7.2 that none of the NWs emitted at, or close to, the free exciton emission line of 1.515 eV at low temperature for ZB GaAs. Surely this is an indication that there are no low temperature radiative recombination confined at the ZB parts of the NW.

For the undoped core GaAs samples, samples A and C, no PL signal could be observed. In contrast, all core-shell GaAs NWs emitted light. The PL spectra for these NWs reveal the importance of the AlGaAs shell as a means of passivation of the free GaAs surface. Surface-related non-radiative recombination is dominating in samples A and C whereas it is greatly reduced in the core-shell samples. However, as the core-shell NWs do not emit at the ZB emission energy, all NWs may likely be affected by another mechanism of non-radiative recombination, inherent to the quality of the ZB phase in these NWs. The most likely reason are native defects related to the Ga-rich growth process and the high growth rate, such as Ga anti-sites or interstitials.

As discussed earlier, type II transitions are possible when electrons from the conduction band of ZB recombine with holes from an adjacent WZ segment. For a heterojunction between bulk WZ and ZB GaAs the corresponding emission energy should be $\sim$1.46 - 1.47 eV depending on the conduction band offset between ZB and WZ GaAs, and will increase for the case of

quantum confined electrons at a SF. Such values corresponds well with the emission energy of NW B2 at 1.478 - 1.480 eV, NW D2 at ∼1.468 eV and the emission energy peaks of NW E1 at 1.472 eV and 1.489 eV, however NW F1 emits at 1.452 eV. Similar spectra have been measured previously for Ga-assisted polytypic ZB/WZ GaAs NWs grown on GaAs substrates [31].

This conclusion is further confirmed by the TEM measurements on NWs from sample D. A couple of TEM micrographs from sample D is presented in figure 8.1 where a mixed ZB/WZ segment is observed at the tip of the NW. As excitation of the tip yielded the highest PL intensity, these TEM images supports the conclusion that type-II transitions are wholly responsible for the PL emission from this sample, and by the similarity of the emission spectra, also from the other samples.

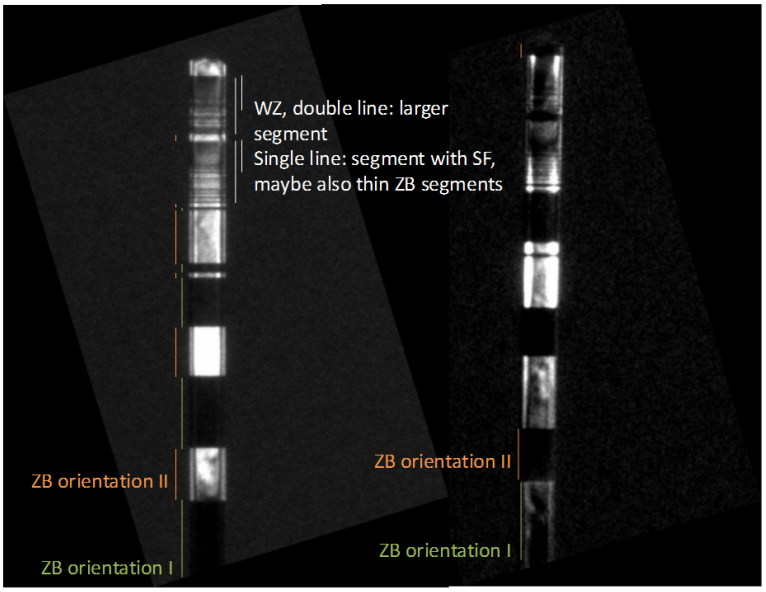

Figure 8.1: TEM micrographs of a representative NW from sample D. The micrograph reveals twins along the wire while the tip transits between ZB/WZ segments as well.

The generally broad linewidths and the fact that at the same excitation level the core-shell NW emission line is broader than for the bare core NW (see figures 7.1 - 7.2 and tables 7.2 - 7.3) is further evidence that the PL arises exclusively from the mixed ZB/WZ segments at the tip of the NWs and is accompanied by band filling and strong non-radiative recombination.

8.2 Power dependence

By studying figures 7.3 - 7.6 and peak emission values from tables 7.4 - 7.7 in the results, it is revealed that the peak emission energy for NW B1 and B2 blue-shifts at low temperature. The blue-shift for sample B indicates a more efficient band filling which in turn signify a slight suppression of non-radiative recombination compared to the other samples. This effect may be partly induced by surface passivation in the presence of doping or due to a decrease in the concentration of native defects neutralized by the dopant. On the other hand, NW D1 and E1 keep more or less the same peak emission energy. The effects of band filling for these NWs are apparently negligible.

In contrast to the NWs from sample B, the peak emission energy of NW F1 red-shifts. NW B1 and B2 behave accordingly to the Burstein-Moss effect by the observed increase of bandgap when the excitation power increases. Indeed, this may be a result of the high doping concentration which could explain why the blue-shift start appearing already at low excitation powers. In general, doped samples should emit less efficiently than the undoped samples as impurities can trap carriers or excitons and promote additional scattering and non-radiative recombination mechanisms. However, sample F is about as bright in PL as the brightest of the intrinsic core-shell samples, i.e. sample D.

Though sample F do not blue-shift, it is seen in table 3.1 contra 3.2 that the doping concentration of sample F is three times lower that in sample B, thus the Burstein-Moss effect may not be observed for NW F1. The red-shift could be explained by EHP effects and bandgap renormalization and also by free-to-bound transitions. Nonetheless, further studies are needed to conclusively identify the origin of this red-shift.

8.3 Temperature dependence

Figure 8.2 presents the data from figure 7.7 with data from WZ [32] and ZB GaAs [33]. The deviation of peak emission of the samples is quite obvious at low temperature but NW B1 and E1 seems to be converging with WZ GaAs at higher temperatures. The fit for NW F1 behaves similarly, but there is a peculiar leap in the peak position consistently occurring in this sample which is an obstacle for achieving a better fit. This discontinuity in the Varshni curve was only observed in this sample. Importantly, it is seen

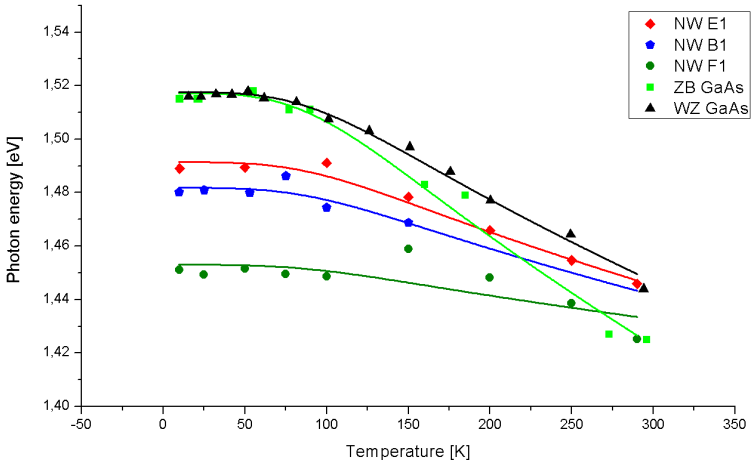

Figure 8.2: Varshni plot of NW B1, E1 and F1 together with empirical data of WZ and ZB GaAs. The experimental data is fitted with equation 5.6 represented by the corresponding colors.

that the peak emission energy decreases slower with temperature than the WZ GaAs for all NWs.

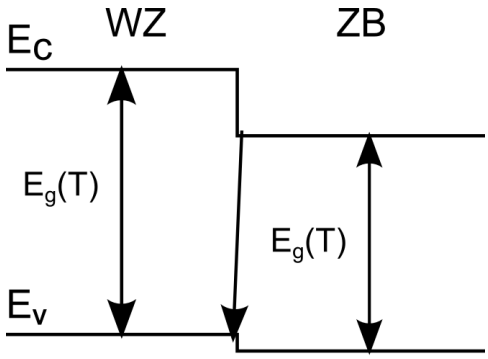

Figure 8.3: A type II heterojunction between WZ and ZB. Each crystal structure has an individual bandgap-temperature relation.

This may be explained by looking at the type II heterojunction between WZ and ZB GaAs, displayed in figure 8.3. As WZ and ZB are different crystal phases, they do also have different lattice constants, thermal expansion coefficients, different bandgap and ultimately different temperature dependence of the bandgap width.

Thus, in view of the fact that the PL emission from the samples studied

in the present thesis is attributed to type-II transitions between WZ and ZB GaAs, it is clear that the emission energy will reflect the band offsets between WZ and ZB GaAs, rather than the intrinsic optical properties of any of the two GaAs phases. This is also the reason for the discrepancy between the results presented here and the literature database on GaAs.

Chapter 9

Conclusion and future outlook

The aim of this work has been twofold - to study self-catalyzed GaAs nanowires by μ-photoluminescence as a means of evaluating and improving the current state of molecular beam epitaxy self-catalyzed nanowire growth at NTNU, and to compare the fundamental optical properties of self-catalyzed GaAs nanowires with their Au-assisted counterparts and bulk GaAs. Evidence is provided that the main photoluminescence emission originates from type II transitions between zincblende and wurtzite GaAs taking place at the nanowire tip.

While it was established that surface passivation by AlGaAs shells greatly improves the optical properties of the nanowires, it was determined that a second mechanism of non-radiative recombination, most likely related to native defects in the zincblende GaAs due to e.g. too large growth rate, impedes photoluminescence emission from the GaAs core. For the self-catalyzed core GaAs nanowires, these defects were not successfully suppressed by application of slower GaAs planar growth rate. Further growth optimization of the self-catalyzed nanowire growth at NTNU is needed in order for the nanowires to represent the optical properties of quasi 1-D zincblende GaAs.

The results of this thesis reveals a vast room of improvement for self-catalyzed GaAs nanowires grown at NTNU. It is beneficial to perform structural characterization by transmission electron microscopy in correlation with photoluminescence analysis. Future nanowires should be grown with shells for surface state passivation and at a slower growth rate in order to avoid formation of native defects.

Bibliography

[1] National Nanotechnology Initiative. What is nanotechnology? http://www.nano.gov/nanotech-101/what/definition.

[2] Guozhong Gao. *Nanostructures nanomaterials: Synthesis, properties applications*. Imperial College Press, (2004).

[3] S. Plissard, K.A. Dick, X. Wallart, and P. Caroff. Gold-free gaas/gaassb heterostructure nanowires grown on silicon. *Applied Physics Letters*, 96(12):121901, (2010).

[4] S Plissard, G Larrieu, X Wallart, and P Caroff. High yield of self-catalyzed gaas nanowire arrays grown on silicon via gallium droplet positioning. *Nanotechnology*, 22(27):275602, (2011).

[5] S. Plissard, K.A. Dick, G. Larrieu, S. Godey, A. Addad, X. Wallart, and P. Caroff. Gold-free growth of gaas nanowires on silicon: arrays and polytypism. *Nanotechnology*, 21(38):385602, (2010).

[6] D. Spirkoska, C. Colombo, M. Heiss, G. Abstreiter, and A. Fontcuberta i Morral. The use of molecular beam epitaxy for the synthesis of high purity iii-v nanowires. *Journal of Physics: Condensed Matter*, 20(45):454225, (2008).

[7] Steffen Breuer, Carsten Pfuller, Timur Flissikowski, Oliver Brandt, Holger T. Grahn, Lutz Geelhaar, and Henning Riechert. Suitability of au- and self-assisted gaas nanowires for optoelectronic applications. *Nano Letters*, 11(3):1276–1279, (2011).

[8] J Todorovic, A F Moses, T Karlberg, P Olk, D L Dheeraj, B O Fimland, H Weman, and A T J van Helvoort. Correlated microphotoluminescence and electron microscopy studies of the same individual heterostructured semiconductor nanowires. *Nanotechnology*, 326(1):012043, 2011.

[9] Dheeraj Dasa Lakshmi. *Growth and structural characterization of III-V nanowires grown by molecular beam epitaxy*. PhD thesis, Norwegian University of Science and Technology, (2010).

[10] R. S. Wagner and W. C. Ellis. Vapor-liquid-solid mechanism of single crystal growth. *Applied Physics Letters*, 4(5):89, (1964).

[11] Roland Diehl. *High-Power Diode Lasers*. Springer-Verlag Berlin Heidelberg, (2000).

[12] H. L. Zhou, Thang B. Hoang, D. L. Dheeraj, A T J van Helvoort, L Liu, J C Harmand, B. O. Fimland, and H. Weman. Wurtzite gaas/algaas core-shell nanowires grown by molecular beam epitaxy. *Nanotechnology*, (20)(41):415701, (2009).

[13] Neil W. Ashcroft and N. David Mermin. *Solid State Physics*. Saunders and Harcourt College Publishers, college edition edition, (1976).

[14] Charles Kittel. *Introduction to Solid State Physics*. John Wiley and Sons, 7th edition edition, (1996).

[15] B. G. Streetman. *Solid State Electronic Devices*. Prentice Hall, 6th edition edition, (2005).

[16] M. R. Brozel and G. E. Stillman. *Properties of gallium arsenide*. INSPEC, (1997).

[17] Bernt Ketterer, Martin Heiss, Emanuele Uccelli, Jordi Arbiol, and Anna Fontcuberta i Morral. Untangling the electronic band structure of wurtzite gaas nanowires by resonant raman spectroscopy. *ACS Nano*, 5(9):7585–7592, (2011).

[18] Mark Fox. *Optical Properties of Solids*. Oxford University Press, 1st edition edition, (2001).

[19] Albert G. Baca and Carol I.H. Ashby. *Fabrication of GaAs Devices*. The Institution of Engineering and Technology, London, United Kingdom, 1st edition edition, (2009).

[20] P.K. Chatterjee, K.V. Vaidyanathan, M.S. Durschlag, and B.G. Streetman. Photoluminescence study of native defects in annealed gaas. *Solid State Communications*, 17(11):1421–1424, (1975).

[21] C. F. Klingshirn. *Semiconductor Optics*. Springer, study edition edition, (1997).

[22] J. Humlicek, E. Schmidt, L. Bocanek, R. Svehla, and K. Ploog. Exciton line shapes of gaas/alas multiple quantum wells. *Physical Review B*, 72(8), (1993).

[23] B.E.A. Saleh and M.C. Teich. *Fundamentals of Photonics*. John Wiley and Sons, 2nd edition edition, (2007).

[24] Inc The MathWorks. Matlab - the language of technical computing. http://www.mathworks.se/products/matlab/?s_cid=global_nav. Version R2008a.

[25] Y. P. Varshni. Temperature dependence of the energy gap in semiconductor. *Physica*, 34(1):149–154, (1967).

[26] T. K. Tran, W. Park, W. Tong, M. M. Kyi, B. K. Wagner, and C. J. Summers. Photoluminescence properties of zns epilayers. *Journal of Applied Physics*, 81(6):2803–2809, (1997).

[27] Spectra-Physics. Millennia pro s-series; diode-pumped, cw visible laser systems, January (2006). Laser manual.

[28] LLC Janis Research Company. St-500 microscopy cryostat. http://www.janis.com/products/productsoverview/SuperTranContinuousFlowCryostatSystems/ST-500MicroscopyCryostat.aspx, (2011).

[29] Ltd HORIBA. Horiba jobin yvon. http://www.horiba.com/scientific/about-us/horiba-jobin-yvon/.

[30] Andor Technology plc. Newton emccd and ccd spectroscopy detectors; a new approach to spectroscopy detection, (2011).

[31] D. Spirkoska, Al. L. Efros, W. R. L. Lambrecht, T. Cheiwchanchamnangij, A. Fontcuberta i Morral, and G. Abstreiter. Valence band structure of polytypic zinc-blende/wurtzite gaas nanowires probed by polarization-dependent photoluminescence. *Physical Review B*, 4(85):045309, (2012).

[32] L. Ahtapodov, J. Todorovic, P. Olk, T.S. Mjaaland, D.L. Dheeraj, A.T.J. van Helvoort, B.O. Fimland, and H. Weman. Manuscript, unpublished, (2012).

[33] P. Lautenschlager, M. Garriga, S. Logothetidis, and M. Cardona. Interband critical points of gaas and their temperature dependence. *Physical Review B*, 35(17):9174–9189, (2087).

Appendix A

Sample information

Table A.1: Sample and NW name replacement for the thesis. The first and third column represents the names and numbers applied at NTNU.

SC no.	Sample name	NW no.	NW name
SC-88	A	N/A	N/A
SC-151	B	NW131, NW221	NW B1, NW B2
SC-162	C	N/A	N/A
SC-109	D	NW2201, NW2211	NW D1, NW D2
SC-138	E	NW3201	NW E1
SC-153	F	NW324	NW F1